



HAL
open science

An In-Depth Look At the Lunar Crater Copernicus: Exposed Mineralogy by High-Resolution Near-Infrared Spectroscopy

Roberto Bugiolacchi, Urs Mall, Megha Bhatt, Susan Mckenna-Lawlor, Marek Banaszekiewicz, Kjell Brønstad, Andreas Nathues, Finn Søråas, Kjetil Ullaland, Rolf B. Pedersen

► **To cite this version:**

Roberto Bugiolacchi, Urs Mall, Megha Bhatt, Susan Mckenna-Lawlor, Marek Banaszekiewicz, et al.. An In-Depth Look At the Lunar Crater Copernicus: Exposed Mineralogy by High-Resolution Near-Infrared Spectroscopy. *Icarus*, 2011, 10.1016/j.icarus.2011.02.023 . hal-00743837

HAL Id: hal-00743837

<https://hal.science/hal-00743837>

Submitted on 21 Oct 2012

HAL is a multi-disciplinary open access archive for the deposit and dissemination of scientific research documents, whether they are published or not. The documents may come from teaching and research institutions in France or abroad, or from public or private research centers.

L'archive ouverte pluridisciplinaire **HAL**, est destinée au dépôt et à la diffusion de documents scientifiques de niveau recherche, publiés ou non, émanant des établissements d'enseignement et de recherche français ou étrangers, des laboratoires publics ou privés.

Accepted Manuscript

An In-Depth Look At the Lunar Crater Copernicus: Exposed Mineralogy by High-Resolution Near-Infrared Spectroscopy

Roberto Bugiolacchi, Urs Mall, Megha Bhatt, Susan McKenna-Lawlor, Marek Banaszkiewicz, Kjell Brønstad, Andreas Nathues, Finn Søråas, Kjetil Ullaland, Rolf B. Pedersen

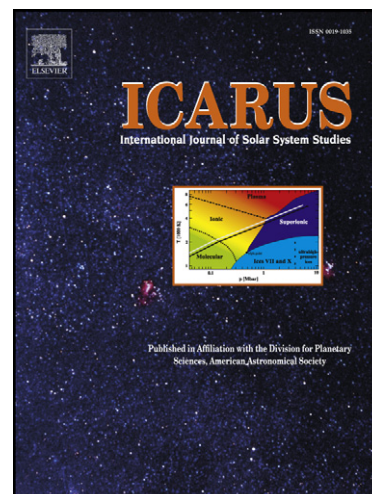
PII: S0019-1035(11)00081-9
DOI: [10.1016/j.icarus.2011.02.023](https://doi.org/10.1016/j.icarus.2011.02.023)
Reference: YICAR 9740

To appear in: *Icarus*

Received Date: 5 July 2010
Revised Date: 18 February 2011
Accepted Date: 22 February 2011

Please cite this article as: Bugiolacchi, R., Mall, U., Bhatt, M., McKenna-Lawlor, S., Banaszkiewicz, M., Brønstad, K., Nathues, A., Søråas, F., Ullaland, K., Pedersen, R.B., An In-Depth Look At the Lunar Crater Copernicus: Exposed Mineralogy by High-Resolution Near-Infrared Spectroscopy, *Icarus* (2011), doi: [10.1016/j.icarus.2011.02.023](https://doi.org/10.1016/j.icarus.2011.02.023)

This is a PDF file of an unedited manuscript that has been accepted for publication. As a service to our customers we are providing this early version of the manuscript. The manuscript will undergo copyediting, typesetting, and review of the resulting proof before it is published in its final form. Please note that during the production process errors may be discovered which could affect the content, and all legal disclaimers that apply to the journal pertain.



An In-Depth Look At the Lunar Crater Copernicus: Exposed Mineralogy by High-Resolution Near-Infrared Spectroscopy.

Roberto Bugiolacchi¹, Urs Mall¹, Megha Bhatt¹, Susan McKenna-Lawlor², Marek Banaszkiewicz³, Kjell Brønstad⁴, Andreas Nathues¹, Finn Søråas⁴, Kjetil Ullaland⁴, and Rolf B. Pedersen⁴.

¹Max-Planck-Institute for Solar System Research, 37191 Katlenburg-Lindau, Germany (bugiolacchi@mps.mpg.de).

²Space Technology Ireland, National University of Ireland, Maynooth, Co. Kildare, Ireland

³Space Research Centre PAS, 00-716 Warsaw, Poland

⁴Department of Physics, University of Bergen, Allegaten 55, N-5007 Bergen, Norway

Abstract

Newly acquired, sequentially spaced, high resolution near-infrared spectra across the central section of crater Copernicus' interior have been analysed using a range of complementary techniques and indexes.

We have developed a new interpretative method based on a multiple stage normalisation process that appears to both confirm and expand on previous mineralogical estimations and mapping. In broad terms, the interpreted distribution of the principle mafic species suggests an overall composition of surface materials dominated by calcium-poor pyroxenes and minor olivine but with notable exceptions: the southern rim displays strong ca-rich pyroxene absorption features and five other locations, the uppermost northern crater wall, opposite rim sections facing the crater floor, and the central peak Pk1 and at the foot of Pk3, show instead strong olivine signatures.

We also propose impact glass an alternative interpretation to the source of the weak but widespread olivine-like spectral signature found in low-reflectance samples, since it probably represents a major regolith constituent and component in large craters such as Copernicus. The high quality and performance of the SIR-2 data allows for the detection of diagnostic key mineral species even when investigating spectral samples with very subdued absorption features, confirming the intrinsic high-quality value of the returned data.

1. INTRODUCTION

The only extraterrestrial planetary materials from known geographical provenance we have access to are lunar. These rocks and soils have been extensively analyzed during the last forty years and employed to constrain and refine plausible models of planetary evolution. By comparing the spectral properties of these samples with remote sensing data it should be possible to investigate the composition and global distribution of lunar surface materials. However, although these samples were taken to represent a broad census of lunar surface materials (e.g. Adams, 1974; Charette *et al.*, 1974), in effect they were sourced only from a relatively narrow mid-latitude belt on the lunar nearside.

The value of this comparative process has been strongly dependent on the available technology at the time of investigation. Ideally, both the laboratory analysis of the samples (e.g. RELAB) and the remotely sensed data should be highly comparable at least in terms of spectral resolution, range, dynamics, illumination, and noise level. Observations of the Moon from Earth in the Near Infrared (NIR) are hindered by atmospheric opacity in key mineralogical diagnostic wavelength centers, but also by modest ground spatial resolution and lunar farside inaccessibility. Relatively recent lunar orbiting instruments have mostly overcome the coverage issue, but have suffered from restricted spectral resolution (i.e. 13 usable VIS-NIR bands, from the Clementine mission) [Nozette *et al.*, 1994] and calibration problems (especially in the NIR).

In this study we present the first detailed scientific application of high-spatial and -spectral resolution (~220 meters, 6 nm) data in the NIR obtained by the SIR-2 instrument on board of the Chandrayaan-1 mission to the Moon (Mall *et al.*, 2009).

We targeted the lunar crater Copernicus because of: its young geological age (Copernican, by definition), still featuring a well-defined ray system; location, within a highly complex geological region; and, it has been the subject of numerous remote-sensing studies (e.g. Pieters, 1982). Although classified as a highland crater, the impact melted, modified, scattered, and uplifted a wide range of lunar materials including highland anorthosite, mare materials, and shocked breccias from previous impact events. Moreover, surface materials within its central peak region display spectral signatures typical of troctolite, a rock type mainly composed of plagioclase and minor olivine, [Pieters 1982; Pieters and Wilhelms, 1985], and normally associated with deeper crustal settings (e.g. Pieters *et al.* 1984).

Copernicus crater's interior will be employed here as a test bed for the mineral diagnostic potential of the SIR-2 multispectral data. Ultimately, new spectral maps of Copernicus' interior (central section) will be presented and form the basis of a broader classification of (NIR) spectral types applicable to other lunar surfaces.

2. COPERNICUS CRATER - FORMATION

2.1. The 'Copernicus' Projectile

It is most likely that the projectile (Durda *et al.*, 1998; Neukum *et al.*, 2001) that hit the lunar nearside with an impact velocity of around 16 km/s 800 ± 15 Ma ago (Bogard *et al.*, 1994; Stöffler and Ryder, 2001) was a ~7 km (Cintala and Grieve, 1998) Near Earth Asteroid of chondritic composition with a mass of approximately 2×10^9 kg (Grieve and Cintala, 1992)(Figure 1[ENTER]). Statistically, the most probable angle of impact θ would have been around 45° (Shoemaker, 1962); even such a high degree of impact obliquity still produces a nearly circular excavation and final crater shape, albeit with consequences for the duration of contact and compression stages (0.62 s against 0.45 s for a vertical hit). This

results in a somewhat reduced depth of excavation as compared with an idealized vertical impact, as well as a potentially asymmetric ejecta distribution. Indeed, at inferred impact angles between 45 to 60 degrees, fresh lunar craters show a preferential accumulation of ejecta on their downrange side (Melosh, 1989, pp. 49-51). It would be tempting to implicate a hypothetical obliquity of impact to explain the asymmetric distribution of materials across Copernicus' surface (**Figure 2**[ENTER], for instance the lower FeO wt% materials mantling the north-western quarter) and the north-south geo-morphological differences (southern floor shortening by 5 km). However, as we shall discuss further, a more plausible explanation for these differences might be sought in the geology and stratigraphy of the target region.

2.2. *The Target*

The projectile that excavated Copernicus struck an area just south of the south-western Imbrium rim (Montes Carpatius, Spudis, 1993, pp.131-164). This is a highly diverse morphological region that rises six kilometres above the lunar mean (De Hon, 1980) and it is characterised by peaks and elevated terrains (massifs). In addition, it is punctuated by valleys and low-elevation corridors that are mostly flooded with mare-like materials. The large size, and occurrence of the Imbrium impact relatively late in the history of the Moon, resulted in the formation of an ejecta blanket which mantled most of the lunar nearside and it is associated with characteristic (radially textured) morphological signatures (the Fra Mauro Formation, e.g. Eggleton, 1964). The Copernicus meteorite hit highland ground admixed with these ejecta materials, a unit called the Alpes Formation (Wilhelms, 1970) and described as being characterized by superficial deposits within a matrix of undulatory terra plains with semi-circular mounds 300-600 m tall with a diameter of about 10 km (Head, 1977; Spudis, 1993). The geo-chemical characteristics of the Alpes Formation have been restrained using both remote sensing techniques and collected lunar samples (Apollo 14 and 15); the data are

shown in Table 7.1 of Spudis (1993, p. 146, and references within) and illustrate the compositional complexity of the surface materials in the Copernicus region.

Thus, the impact occurred on a highly stratigraphically complex and heterogeneous region of the lunar surface, mostly composed of feldspathic highland materials rather than mare (McCord *et al.*, 1972), as the (alleged) direct and remote-sensing analysis of materials belonging to the Copernicus ray system has suggested (Pieters *et al.*, 1985). The lunar region where the impact occurred has been recently proposed to be petrographically relabeled as Procellarum KREEP Terrane (Hasking *et al.*, 2000; Jolliff *et al.*, 2000) based on Clementine (VIS-NIR images) and Lunar Prospector (Th abundances) data. Nonetheless, Copernicus (along with a few other large craters) stands out by its exceptionally low thorium concentrations in respect to the region's average (e.g. Gillis and Jolliff, 1999).

To summarize: materials pulverized, re-melted, shocked, and excavated by the impact would have originated from (top down): 1] a thin layer of mare basalt (~250 m, De Hon, 1979) post-dating the Imbrium event; 2] overlying (or mixed with) noritic ejecta layers from the Imbrium event itself (estimated to be between 0.4 to 3.0 km thick, McGetchin *et al.*, 1973; Pike, 1974); 3] a KREEPy layer, belonging to the regional Procellarum KREEP Terrane (i.e. ; Hasking *et al.* 2000; Jolliff *et al.*, 2000; Lawrence *et al.*, 1998); 4] superposed on a highly brecciated mafic-rich substratum with an increasing olivine/pyroxene ratio with depth (Pieters *et al.*, 1994; Pinet *et al.*, 1993;).

2.3. The Impact and Modification Stages

The 'Copernicus' impactor hit the lunar surface with an estimated kinetic energy of about 9.6×10^{22} joules, which was mostly transferred to the target rocks. Within a second, shock waves in excess of 300 GPa (Ahrens and O'Keefe, 1977) propagated through the projectile (a

‘release wave’) and the target rocks, resulting in vaporization of the former and compression, heating, and displacement of the latter (Melosh, 1989). Estimates relating to this stage of crater formation are based on computation and up-scaling of laboratory and terrestrial impact studies (e.g. O’Keefe and Ahrens, 1982) and suggest figures of overall mass displacement in the range (for a Copernicus-size impact) of 3.4×10^{16} kg, mass of melt $\sim 2.0 \times 10^{15}$ kg, and mass of vapour $\sim 2.0 \times 10^{14}$ kg. A more in-depth discussion on the geological and petrological aspects and consequence from the impact can be found in Chapter 6.1.

Given the nearly instantaneous melting/vaporization of the projectile (culminating as a minor fraction of the vapor plume and melt materials), the actual mechanical excavation of the crater was carried out by expanding shock waves propagating through the target. The dynamics of the excavation stage are usually framed within the somewhat idealized concept of a transient crater since this is not scale-related and can thus be applied to a wide impact spectrum (Dence, 1968; Grieve and Cintala, 1982; Grieve *et al.*, 1981; Melosh, 1989, Chapter 5).

After the initial contact and compression (which produced ejecta from near-surface materials, mostly in the shape of discrete fragments travelling at high velocities), the release shock wave continued to expand downwards causing deep fracturing along with some melting of target materials [a melt that would eventually overlay the expanding transient cavity (~ 200 m thick), Cintala and Grieve, 1998]. At the same time a symmetrical ejecta curtain would have carried some of these melt materials outward to significant distances, along with a fraction of shocked rock deposits.

In lower pressure zones, materials pushed outward caused the radial uplifting of near-surface rocks to form the rim of the transient crater. The ‘final’ transient cavity diameter for

Copernicus was probably in the region of 74 km in diameter (Cintala and Grieve, 1998; Schmidt and Housen, 1987) and 4.4 km in depth (Wood and Anderson, 1978), giving a volume of about $9.4 \times 10^6 \text{ km}^3$. Within less than a minute (Melosh, 1989, p. 123) the excavation process was completed and the modification stage began.

This stage is largely gravity controlled (Gault *et al.*, 1975; Quaide *et al.*, 1965) and, in craters the size of Copernicus, the process involves the concurrent relaxation and collapse inward of the compressed transient crater rim and the uplifting of deeply sited materials below the impact zone. This type of crater, which typically is characterized by well-developed wall terraces, a flat floor, and a central peak structure is described as 'complex', and in particular, according to Wood and Anderson (1978), Copernicus is classified as a TYC (Tycho), LPL Class 1 (fresh) crater. The exact dynamic and temporal development of the final configuration of a complex crater is not well constrained. For instance, it is not clear if the central uplifting starts before the ending of the excavation phase, while the rim is still building, or subsequently. Nevertheless, crater wall failure is thought to be linked to the inward movement of the crater sub-floor in response to central peak surfacing (Pike, 1980) and consequent concentric faulting at depth. Scallops, terraces, scarps and irregular sloping surfaces are the morphologic consequences of these dynamic processes.

3. THE LUNAR SURFACE - BACKGROUND

3.1. Lunar Surface Materials

Lunar surfaces are mostly covered by regolith (e.g. Oberbeck *et al.*, 1973), which is highly compacted at a subsurface level and considered to represent the local underlying mineralogy (Gault *et al.*, 1974; Taylor, 1975). In comparison to many other planetary bodies, the Moon is significantly depleted in volatiles (e.g. H_2O , CO_2 , OH^- , etc.); the result is in a relatively

simple mineralogy comprising a few dominant phases (feldspars, pyroxenes, olivines, ilmenite, and oxides). These minerals represent the building blocks of the three major groups of rock types (or clast fractions) found on the lunar surface (Taylor, 1982; Taylor *et al.*, 1991; also lunar highland classification scheme of Stöffler *et al.*, 1980): [1] Mare basaltic lavas, similar but not identical to terrestrial lavas; [2] Pristine highland rocks including (a) Ferroan Anorthosite (FAN), (b) the Mg-suite, and (c) KREEP rocks; and [3] Breccias, representing the bulk of the lunar rock samples returned by the Apollo missions and subdivided into many groups of which polymict breccias are by far the largest (Taylor *et al.*, 1991).

The three key mafic minerals that are present nearly ubiquitously in lunar sample materials are the two pyroxene phases (low- and high-calcic pyroxenes) and olivine. Their distribution in rock samples is diagnostic of diverse melting regimes, whereas, for instance, a high olivine fraction suggests a relative deep crustal, or even a mantle origin. The occurrence of high-calcium clinopyroxene (cpx) points instead to a later fractionation of relatively more evolved melts [Longhi (1977, 1981); Schnetzler and Philpotts, 1971; Snyder *et al.*, 1992; Taylor, 1982; Taylor and Jakes, 1974].

The mode of occurrence and spatial/volumetric distribution of these phases provide a key to a better understanding of the evolution of the lunar crust, with obvious implication for the lower strata and the overall thermal evolution of the planetary interior (see for instance Hess, 1994 for a discussion on lunar troctolite petrogenesis).

3.2. The Optical Properties of the Lunar Surface Materials

The surfaces of airless bodies including the Moon are relentlessly bombarded by micrometeoroids, solar wind particles, and high-energy cosmic rays (a process named ‘space weathering’). The result is a continuous reworking and mixing (‘gardening’) of the exposed

materials through melting, sputtering, vaporization, and pulverization of particles. These processes generate: (a) agglutinates (e.g., Rode *et al.*, 1979), glass bonded debris of rocks and minerals (up to several tens of percent in mature regolith, e.g. McKay *et al.*, 1991); (b) individual grain effects (such as rare gas implantations and glass splashes); (c) and nanometer-scale particles of metallic iron (npFe^0) implanted within agglutinates and as spatter on individual soil grains (Baron *et al.*, 1977; Housley and Grant, 1975, 1977; Hapke, 1973; Hapke *et al.*, 1975). Nanophase iron is found in two distinct size ranges which affect the regolith's optical properties differently: (1) npFe^0 , present as thin patinas on irradiated grain rims, is on average about 3 nm in diameter (range between 1 to 15 nm; Keller *et al.*, 1998; Keller and Clemett, 2001; Wentworth *et al.*, 1999) and it is linked to the increase in spectral reflectance in the NIR (e.g. Cassidy and Hapke, 1975; Morris, 1980), a phenomenon often referred to as the 'reddening of the continuum slope'; (2) larger nanospheres up to several hundred nanometres (Housley *et al.*, 1973; James *et al.*, 2002; Keller and Clemett, 2001), which are found in agglutinates: their accumulation with time is linked to soil darkening and consequent weakening of spectral features.

3.3. Remote Sensing

Recent findings (i.e. 'water' on the Moon, Clark, 2009; Pieters *et al.*, 2009; Sunshine *et al.*, 2009) have shown there is still much to learn about our satellite and how remote sensing can help overcome the geographical, and consequently compositional sample bias, of the returned samples.

Remote investigation of planetary surfaces can be carried out by several means, ranging from spectrography to radar. Here we explore the reflectance characteristics in the near infrared range of the materials exposed within the Copernicus crater edifice.

The component of the incident solar radiation that is not absorbed is scattered back into space by one or more particles. The mineralogy, shape, and size of the grains are the main factors dictating both the intensity and the spectral location of the (eventual) absorption feature(s) (e.g. Burns 1993). Since reflected radiation carries information on the average mineralogical composition and other physical variables of the exposed materials, remote sensing offers the potential of carrying out geological surveys of otherwise inaccessible planetary surfaces (e.g. Pieters, 1986).

The spectral absorptions characteristic of mineral crystals (e.g. Bell *et al.*, 1975; Burns, 1970; Burns and Vaughan, 1975) and spectral reflectance of powdered rocks, minerals, and soils (e.g. Adams, 1974, 1975; Hunt and Salisbury, 1970) have been well studied and constrained. Multispectral telescopic observations of landing sites on the Moon support, over a broad scale, comparative studies involving the laboratory analysis of corresponding lunar samples (e.g. McCord and Adams, 1973).

Figure 3[ENTER] (Charette and Adams, 1977) shows one of the many available examples of comparative laboratory spectrograms using mineralogical components derived from the Apollo sample pool (e.g. Pieters *et al.*, 2000).

4. SIR-2 SPECTROMETER

4.1. The Instrument

Our spectral analysis of the Copernicus crater is based on new data acquired by the SIR-2 instrument on board the Indian Chandrayaan-1 mission, a second-generation near-infrared spectrometer (Mall *et al.*, 2009). The SIR-2 instrument is a grating-based, compact, high-resolution point spectrometer operating in the 0.9–2.4 μm spectral range sampled by a 256

channel pixels array (giving a 6 nm spectral resolution). It incorporates a thermally stabilized InGas detector (Mall *et al.*, 2010) which delivered consistent, reliable, and comparable spectral readings. The SIR-2 field of view from 100 km altitude translates into a ground sampling resolution of approximately 220 m. The instrument was operational between January and August 2009 from orbital altitudes of 100 and, towards the untimely end of its mission, 200 km.

SIR-2 surveyed the Copernicus edifice on several occasions, criss-crossing the crater longitudinally. In particular, orbits 1095 and 1929 dissected the full diameter of the excavation at around 20° W, thereby collecting NIR readings of the mineralogically-sensitive central peak mountains. From these two orbits we selected orbit 1095 for the present investigation, due to its ideal observational characteristics (optimal phase angle, 30°), optimal observational altitude (100 km), and accurate ground correlation coordinates **Figure 4**[ENTER].

During orbit #1095 the SIR-2 instrument took 174 individual spaced readings within Copernicus' crater interior (with gaps of around 330 meters) of slightly elliptical footprints along the described orbital path, in effect sampling a strip of terrain ranging from the northern to the southern rim crests (in total about 5.5 km²). Each reading thus represents the average near-infrared absorption/reflectance characteristics of the sampled surface materials within an area of ~38,710 m².

Data reduction and calibration procedures are described in Mall *et al.*, (2010).

5. DATA ANALYSIS

5.1. Summed Reflectance (SR)

Summed Reflectance (SR) represents the arithmetical sum of all post-calibration reflectance values for each of the 256 interrogated pixels (i.e. discrete wavecentres), indicating in essence the overall NIR reflection intensity of each sampled point. **Figure 5** presents these SR values superimposed along the observational orbital path to highlight variations (using the north floor area as an ‘average’ reflectance). The north rim (RN) region displays several ‘bright’ exposures (we use the terms ‘bright’ and ‘dark’ to describe higher and lower summed values in the NIR SR data, not albedo) associate with the steeper crater rim walls: gravitational slumping of surface materials exposes less weathered and crystalline materials, which display higher reflectance properties. The materials on the flat terrace steps are similar in brightness to the crater floor averages.

Sample Point (SP) 9914 represents the highest reflectance spot in the region with no obvious morphological correspondence. It is located on what appears to be a lava channel flank (levee) and its high reflectance characteristics might be the result of topography (low phase angle in respect to the SIR-2 viewing geometry), inherent geological properties (higher reflectance materials, such as troctolite), or a combination of both.

The NIR SR levels around the Central Peak area (CP) follow the topographic contour of this mountainous area (Fig. 5) including a sudden drop in reflectance corresponding to the shadowed flank of the main peak (Pk1, from bright SN 9978-9 to dark SN 9981).

The south floor (FS) area is smaller and more irregular (i.e. more hummocky and undulating) than the northern half although the overall summed reflectance level remains comparable. As the topography changes with the onset of the southern rim (RS) we notice a gradual, southwards decline in reflectance values culminating with the lowest recorded readings (SN

10031-32). These coincide with a flat and low lying area infilled with, presumably, mature mare-like materials.

5.2. Spectral Variations – ‘Shape’

The spectra collected within the Copernicus diameter are presented in **Figure 6a** (here shown as best fit lines for ease of comparison).

We have highlighted representative spectral ‘shapes’ in **Figure 6b** along with the original reflectance values for each pixel (before best-fit lines are derived). As one can see, readings above $2.2\ \mu\text{m}$ suffer from higher data scattering (noise); this is caused by ‘*quantum fluctuations*’, which occur when the statistical photon count falls below a threshold and the measuring errors grow (Janesick, 2001). The diagnostic absorption features of the silicates under investigation here are only marginally affected since the diagnostic band centers in this spectral region fall mostly within the $1.9\text{-}2.2\ \mu\text{m}$ range.

The brightest NIR spectra belong to the main central peak’s north-eastern slope (SN 9978-9, Pk1, Fig. 5); for comparison we also show SN 9981 in the same figure (Fig. 6b) from the shadowed flank one kilometer away.

SN 10040 from the southern rim is characterized by a deep, broad $2\ \mu\text{m}$ absorption feature; this is typical of several southern rim spectra and it will be discussed further in this work. In contrast, SN 10014 represents the flattest spectrum from within the crater.

The darkest spectra SN 10031-2, as highlighted in Ch. 5.1, stand out from the rest of the samples (Fig. 6a) and confirm the exceptional high absorption properties of the surveyed materials.

The direct comparison between laboratory sourced spectra of potentially comparable lunar mineralogical assemblages (e.g. Fig. 3) and our remote sensed data highlights key spectral differences of spectral behavior; SIR-2 point spectrometer readings represent the average reflectance properties of about 0.04 km² of exposed regolith, potentially including breccias and rare crystalline mafic exposures, but mostly comprising of pulverized and admixed lunar materials (except for the central peaks, which are mostly brecciated rocks, e.g. Pieters 1982). We can start drawing first-order comparisons with laboratory spectral data, as from Fig. 3: SN 9978-9 resemble the troctolite sample (A17, Inside Chip 76535,35, Charette and Adams, 1977) while SN 10040 appears similar to the noritic anorthosite (A17, IC 72215,101). Both interpretations are highly plausible, since they belong to the olivine-rich central peak region and the strong pyroxene signature samples on the southern rim respectively.

To facilitate direct spectral comparisons we produced **Figure 6c**[ENTER], which represents the normalized reflectance values scaled at 1.616 μm (instrument pixel #104). While discarding valuable information on absolute reflectance, we can now compare differences in spectral ‘shapes’ directly, focusing on mineral absorption characteristics. For instance, spectra SN 9978-9 and 9981, which appeared unrelated in Fig. 6b, are here similar, suggesting a shared mineralogy masked by different overall reflectance strength, possibly due to shadowing factors (illumination angle), grain sizes, morphology, or a combination of these factors.

SP 10014 ‘stays’ virtually featureless, probably because of its high maturity, high concentration of opaque materials, or low Fe²⁺ content.

Next we compared the normalized spectra for each sample point and qualitatively classified them according to overall similarity in ‘shape’. The 174 spectra were observed to belong to

six main groups, here classified from ‘ α ’ to ‘ ζ ’, as shown in **Figure 6d**[ENTER]. The progressive alphabetical nomenclature mainly reflects a strengthening of the 2 μm absorption feature (α representing the weakest and ζ the deepest). The interpretative translation of these groups into defined mineralogical groups is not straightforward; nevertheless, we see that α corresponds to sampled areas with the weakest overall absorption features, probably representing more mature materials and/or richer in opaques; β differs from α for a slightly less steep continuum and a faint, albeit stronger 1 μm feature; γ and δ are apparently similar but the former, when observed in detail, displays a much stronger absorption around 1.08 μm and a flatter 2 μm spectrum. We shall investigate the γ group in much detail later in the study since this kind of spectrum has been associated with the mafic mineral olivine within the central peak region; finally, ϵ and ζ both show strong 2 μm features and overall comparable ‘shapes’, but differing in absorption strengths.

Figure 7[ENTER] shows the distribution of these preliminary spectral types across Copernicus. The predominant type is represented by α (~60% of all samples) and it is found across the northern rim and crater floor and probably represents impact melt material not dissimilar to mare basalts. Whilst the crater floors [as per our division between the northern (FS) and southern (FN) halves] share similar spectral characteristics, the rims and central peak area differ substantially: the northern rim (RN) is punctuated by materials showing a spectral δ ‘shape’, hinting at an admixed composition including both pyroxene and olivine as the predominant mafic components; the southern rim (RS) instead features the ‘dark’ β spectral type towards the crater centre, but the stronger 2 μm absorption types (ϵ and ζ) as we move southwards. ϵ is also found just north of Pk3 and probably associated with fresh ejecta from a small optically bright crater in the area; γ is detected only within the crater peak (CP) region and, as commented earlier, linked with olivine-rich materials.

5.3. Mineral Spectral Parameters (MSP)

A NIR spectrum of a relatively large geological area represents the sum and complex interactions of individual spectral properties of a heterogeneous admix of different lithologies and mineralogies. There have been several approaches in trying to unscramble and decipher summed spectra ranging from direct spectral characteristics comparisons with laboratory data (e.g. McCord *et al.*, 1981; Smrekar and Pieters, 1985) to sophisticated inverse deconvolution models such as MGM (e.g. Isaacson and Pieters, 2010; Sunshine *et al.*, 1990)

Reflectance band strength ratios is an investigative method widely used in the UVVIS range to derive quantitative (wt %) estimates of key diagnostic oxides (i.e. Lucey *et al.*, 1998; Wilcox *et al.*, 2005). In this study, we applied mineral spectral parameters similar to those derived to investigate the distribution and relative abundance of key mineralogical mafic phases on the Martian surface (Pelkey *et al.*, (2007), based on data collected by the OMEGA/Mars Express instrument (Bibring *et al.*, 2005) . Pelkey *et al.*, (2007) cautioned that remote sensing spectral parameters cannot easily be translated into quantitative estimates of mineralogical abundances since soil reflectance characteristics are influenced by several physical variables (particle size, texture, surface texture, etc.) that are challenging to extricate, isolate, remove, and, crucially, quantify using today's analytical techniques. Here we do not attempt such a complex task but offer this analysis as complementary to our investigation and classification of lunar spectral signatures in the NIR.

The pyroxene indexes (**Table 1**) in essence compare the relative reflectance values of each sample point in key wavelength regions: the '1 μm ', NIR albedo (1.329 μm), shifted NIR albedo (1.468 μm), and the 'typical' opx and cpx band centers (1.814 and 2.067 μm respectively). The olivine index focuses instead on the lower NIR wavelength centers close to

the 1.04-1.10 μm range, the strongest spectral absorption feature of the mineral and its variations in relation to the mid-point wavelength at 1.616 μm (for the SIR-2).

Figure 8[ENTER] plots the combined results of the three index parameters. We have also drawn arbitrary ellipses to highlight trends and exceptions among the spectral points within geographical variations. Overall, the crater floor appears spectrally homogeneous although with a tendency for the southern rim to be cpx-rich than the northern equivalent, and showing a weaker olivine signature too. There are some exceptions though, most notably SN 9962-3: these are two NIR 'bright' points near the central peak region with a mafic absorption signature similar to cpx-rich materials as found on the southern crater rim. Fig. 5 shows this sampled area to be in the proximity of a small crater with (immature?) high albedo ejecta. In several remote sensing investigations the more calcic varieties of pyroxene are detected in correspondence with brighter and fresher exposures; this raises the question if we are observing real mineralogical differences in terms of pyroxene species or a spectral artefact related to maturity and the presence of more crystalline materials. Assuming that materials exposed by fresh impacts or gravitational slumping are relatively 'unspoiled' and a truer spectral signature of the local mineralogy, does weathering affect the *apparent* blue shift of the 1 and 2 μm absorption features? Alternatively, is this a consequence of actual mineralogical changes in the exposed soils, i.e., is there a known geophysical mechanism that selectively suppresses or even progressively remove the pyroxene calcium-rich phases?

The spectral ratios of materials from the terraced areas suggest an olivine-enriched northern rim in respect to the opx-rich southern half. This mirrors the trend observed in Fig. 7 and in particular, it confirms the presence on the southernmost section of the rim of surface materials displaying very strong spectral indicators of clinopyroxene-rich mineralogy (Fig. 7, 'ζ'; Fig 8, i.e. SN 10052-10040-10047).

Fig. 8 shows that most of the central peak region spectra are similar to those from the northern rim region but with notable exceptions, as per samples 9978-9 (CP2), 9967-9 and 9980 (CP1). CP2 corresponds to the main central peak Pk1 (Fig. 4) and the strongest overall reflectance of this survey (Fig. 5). Samples 9967-9 belong to the terrain just west of Pk3, thought to correspond to remote-sensed lunar materials with the strongest olivine presence (i.e. dunite/troctolite; e.g. Pieters 1982). The highest olivine index is represented by SN 9980, which belongs to the Pk1 summit.

Overall, these indexes appear to be in broad agreement with our qualitative classification of the spectral type (Figs. 6d and 7). In order to compare the MSP indexes with the other investigative methods employed in this study, we have subdivided the plotted data into five arbitrary groups (inset in Fig. 8). Clearly, the boundaries between spectral types have been subjectively chosen and might be redrawn using any other qualitative parameter (for the meaning of each group's name, please see figure caption).

5.4. Comparative Normalization Analysis (CNA)

We have developed a comparative normalization routine to automate the spectral shape analysis and classification of the SIR-2 NIR data. The depth of absorption parameter is one of the key elements for estimating the mineralogical mode of the surveyed surface area; however, since a consistent and reliable technique has yet to be developed to translate spectral data into absolute mineralogical fractions, we have chosen to concentrate on the absorption band centre shifts and comparative behavior as a mean of tracking compositional trends. Again, one must stress how an absorption feature width, depth, and centre in the NIR represent only the summed absorption behavior of mineral phases containing Fe^{+2} within their crystal framework, therefore not representing any other mineral devoid of this ion.

Furthermore, a strongly absorbent mineral phase, such as orthopyroxene, may swamp most spectral features of other key components such as olivine, pyroxene, spinel, and (especially) plagioclase even if present in significant fractions.

To illustrate the Comparative Normalization Analysis (CNA) method, we have employed the spectral sample 9978 as a case study (**Figure 9a**[ENTER]). This spectrum belongs to the Pk1 mountain (Fig. 5) and found to display absorption features associated with the presence of olivine as the main mafic mineral phase (Ch. 5.3). The entire sample pool used in this study is first normalized as in Fig. 6c. We have selected 18 band centers known to represent the diagnostic absorption features of key mineral species (e.g. Adams, 1974; Burns, 1970) and extracted their mean reflectance values of qualitatively selected neighboring pixels (for instance, 1 μm is represented by the mean of 0.9977, 1.0035, and 1.0093 μm reflectance values) (**Figure 9b**[ENTER]). **Figure 9c**[ENTER] plots the relative reflectance values for spectrum SN 9978. When the same data for all the spectra are plotted along the orbital path within Copernicus (**Figure 10a**[ENTER]), one can follow the variations in reflectance behavior relating to each of the selected 18 wavecentres (as per Fig. 9b).

By further normalizing the obtained spectral data (as in **Figure 10b**[ENTER]) we are now able to plot and compare numerically variations in absorptions for the whole 174 spectral profiles across the diagnostic bands. This process also has the advantage of minimizing the 'red continuum' effect that causes the reflectance to increase exponentially towards the 'red' part of the NIR spectrum. We must emphasize that this 'double normalization' technique produces meaningful results only for large and consistent data sets, such as the 174 SIR-2 reflectance samples used in this study.

For ease of comparison the newly normalized data was then arbitrarily scaled from 1 to 10 (**Figure 10c[ENTER]**), where the smaller numbers represent the (relatively) lowest reflectance values (i.e. strongest absorptions) within each sample.

We further averaged and grouped our reflectance values down to seven key wavelength ranges (see **Figure 10c[ENTER]**) as a first order absorption diagnostic tool. If we follow our example for SN 9978 (from Figs. 9a to 10d) we see how we progressively zoom in to the key spectral characteristics of this sample, which in Fig. 10d shows strong absorption features in the 1.05-1.10 μm range ('C'), followed by 1.25-1.30 μm ('D') and $>2.00 \mu\text{m}$ ('F'; 'G' will be discussed later). This spectral signature is similar to laboratory-sampled lunar soils of troctolitic character (see Fig. 3) and confirms, at least on a comparative basis with other studies (i.e. Pieters 1982), the validity of our approach. We introduced a new classification code ("Spectral Type", **Table 2[ENTER]**) reflecting the relative strength of absorptions as derived from Fig. 10d where the first (capital) letter represents the most significant (not necessarily strongest) absorption (in the case of SN9978 it becomes 'Type Cdg1'). Note: 'G' (2.35 μm) is always given a lower denomination since most spectra tail off in this region and, crucially, the data suffer from high noise levels (see Ch. 3.3).

The "Mineralogical Interpretation" in Table 2 is largely derived from the "Spectral Type" classification, but not always: in some cases it was necessary to refer back to the more detailed '18-Bandcentres' data to improve interpretation. In general, the dominant absorption feature imposes the interpreted mineralogical 'character' and description used in this classification. For instance, 'D' type (as in the case of 'Dcag') are mostly classified as "mature" soils since the diagnostic 1 and 2 μm signatures appear subdued in comparison to the 1.25-1.30 μm range ('D'). Similarly, a prominent ' $>2 \mu\text{m}$ ' feature ('F' type), is strongly

diagnostic of the presence of clinopyroxene, hence classified as “cpx”. As always, there are exceptions: we have also classified ‘Af3’ (SN 10029-31) in the same “cpx” group since a concurrent strong absorption at $<1 \mu\text{m}$ is also associated with this pyroxene phase.

There are several factors complicating an ‘automatic’ association of spectral absorption features with known mineral admixes. For instance, most surface materials were found to display “mature \pm x” spectral characteristics (where x may represent either pyroxene [px], orthopyroxene [opx], or olivine [ol]) and associated with weak diagnostic absorption features (Table 2). We discussed the significance of space weathering on the reflectance properties of lunar soils in Ch. 3.2, but we also need to take into account the absorption effects in the NIR of impact glasses, which are of particular significance given the high fraction of glass produced by the Copernicus impact. The presence of impact glasses within the regolith produces a broad one-micron absorption (Bell *et al.*, 1976; Denevi *et al.*, 2008; Wells and Hapke, 1977) that can be easily misinterpreted as representing a specific mafic phase. Moreover, when more than one diagnostic mineral are present, the interaction between the single absorption features are summed and become difficult to extricate. For instance, opx-olivine mixtures causes the $1 \mu\text{m}$ band centre to ‘migrate’ towards longer wavelengths with increasing olivine fractions in a non-linear fashion. Given the weaker absorption properties of olivine, the combined 1 micron band centre only ‘crosses’ the $1 \mu\text{m}$ threshold for opx/ol ratios >0.25 (Singer, 1981). Similarly, opx/cpx mixed phases remain below the $1 \mu\text{m}$ threshold for opx/cpx ratios >0.25 . The “Mineralogical Interpretation” descriptions we offer in Table 2 reflect our best efforts to date. For instance, we were undecided whether to use the generic term “mature” or “impact glass”. Maybe a third and better description will be found. There is little doubt that as we progress through our spectral investigations and apply the “CNA” method to other lunar environments we should gradually gain a better insight into the

NIR spectral characteristics of surface materials and fine-tune our interpretative and classification efforts.

Figure 11[ENTER]) brings together the results from our three investigative methods for ease of comparison (Fig. 11A from Fig.5; Fig. 11B from Figs. 7 and 8.; Fig. 11C from Table 2).

6. DISCUSSION

6.1. Impact Rocks, Metamorphism, and Melts

The length of the contact stage for an impact that produces a 100 km crater is around half a second (Melosh, 1989, also this work Ch. 2.3). During this brief time the target materials experience peak pressures of the order of hundreds of GPa (300-400 for Copernicus) and post-shock temperatures in excess of 2000°C, given that 50 % of the kinetic energy of the impact is transformed into thermal energy. This heat is far above the melting point of most rocks and their mineral constituents and results in the instantaneous liquefaction of target materials. Based on the equation given by Grieve and Cintala (1992) the Copernicus impact would have generated around 900 km³ of melt (calculated from the diameter of the transient crater), or nearly 4-5 times the volume of the impactor itself (enough to produce a 200 meter melt layer on top of the transient cavity). This initially nearly-spherical body of melt would immediately be incorporated in the outward flow of materials during the excavation phase of the transient crater (e.g. Dence, 1971; Grieve, 1987; Grieve *et al.*, 1981). The mobile melt would have progressively assimilated various clast materials, thereby leading to faster cooling of the mix and the formation of a heterogeneous array of distinct units ranging from clast-rich impact melt breccia (Dence, 1971; Grieve *et al.*, 1977) to clast-poor melt (Simonds *et al.*, 1976, 1978). **Figure 12A**[ENTER]) shows signs of fluidic flow patterns of melt materials emplaced along the northern rim terraces (indicated by arrows) and draining

downwards onto the crater floor. Since the flow pattern ceases at the point of contact with the crater floor, we can assume that the solidification of the crater floor melt veneer occurred either concurrently to the terrace melt intake or subsequently. Nevertheless, the impact melts on the crater floor must have cooled relatively quickly as cooling cracks are a very common recurrence (**Fig. 12B**) (i.e. Hawke and Head, 1977; Morris *et al.*, 2009).

Since the pressure gradient falls off rapidly away from the impact point, it produces a continuous range of differently shocked materials. A detailed discussion of shock-metamorphic effects in rock and minerals is beyond the scope of this paper (see Stöffler 1984; Stöffler and Langernhorst, 1994), and here we focus only on the surface materials likely to be observed within Copernicus by remote sensing.

Within the crater interior, not including the central peaks of the complex crater, we find a chaotic and heterogeneous mix of various types of allogenic breccias and autochthonous melt rocks. These materials may include: shocked and unshocked materials caught up in the collapse of the transient crater during its modification stage; the fall-out of vertical or near-vertical ballistic ejecta; and impact melt. However, the (visible) uppermost stratum of the floor of large impact craters is thought to be composed mainly of impact melts overlying brecciated rocks (i.e. **Fig. 12C**). The finely pitted appearance of the crater floor (e.g. Fig. 12A) and the smoothen rim outline of the larger impacts (**Fig. 12D**) suggest a considerable debris rain of melt-rich materials that had been ejected at high angles and fallen back into the crater (Dence, 1971; Hawke and Head, 1977) before the melt veneer had completely solidified.

However, crater rim zones are petrologically more diverse and would include materials displaying various stages of impact metamorphism, such as polymict lithic breccia, with overlying melt-bearing breccia (suevite).

The mineralogical description of 'impact melt' is somewhat vague and encompasses any target rock which has undergone a rapid, or nearly instantaneous, melting and subsequent re-solidification. The speed of cooling of the melt is governed by the same mineralogical constraints and processes characteristics of igneous rocks (chemical composition, cooling speed, xenoliths inclusions, etc.). This is why, even on Earth, it is sometimes difficult to distinguish in the field between an impact melt and a volcanic (extrusive) rock (Dence, 1971; Grieve *et al.*, 1977; Grieve and Cintala, 1992; Schuraytz *et al.*, 1994), although inclusions of shock-metamorphed clasts, together with evidence of higher-than-normal crystallization temperatures and environment of formation, accompanied by traces of projectile materials, often reveal, under laboratory conditions, the true petrogenesis of the sample.

Looking at the surface of a typical floor within a larger lunar crater we note low albedo materials both mantling and embaying the breccias that infill the excavation. LROC images [obtained using a high-resolution camera on board the LRO NASA lunar mission, (<http://wms.lroc.asu.edu/lroc>)] offer an unprecedented look at this stratigraphy: **Fig. 12E** shows a collapse feature within the north floor revealing the layered structure of the Copernicus floor, including the surface mantling of presumably fractionated melt resembling mare (i.e. basaltic) materials, overlying strata of increasingly clast-rich materials, impact breccias of anorthositic composition (light color to white). This image, along with others, e.g. Fig. 12D, suggests that the mobile melt veneer to be thinner than previously thought, at least locally, and in the order of tens of meters.

6.2. Crater Rim

The Copernicus modification stage resulted in the peripheral collapse of the crater rim, accompanied by extensive slumping of rock materials along concentric normal faults, forming depressed rings (ring grabens), scarps, and terraces that became proportionally narrower towards the centre of the excavation (Melosh, 1989, e.g. 8.3.5, p. 147). In work carried out since the early 1960s, in particular by E. M. Shoemaker, researchers have found that approximately half of crater rim materials are composed of fractured, shocked, outwardly and upwardly displaced impact target rocks. Before gravitational collapse, Copernicus' transient crater rim would have been uplifted several times and incorporated breccia-like materials through dike emplacements, which then became part of the rim basement.

The upper part of a typical crater rim is composed of ejecta debris, thrown out at high velocity from the impact area: consequently, it mostly reflects the composition of the target rocks, although shock metamorphosed and brecciated (Melosh, 1989). Additionally, since the maximum depth of excavation would have been reached before the attainment of the maximum diameter (e.g. O'Keefe and Ahrens, 1994), this process would have resulted in the rebounding of the central region and a consequent surge of hot fluid materials towards the expanding cavity walls. Mare-like materials, featuring low albedo and lightly cratered patches can be observed in low-topographic corridors, ponds, and hollows at the foot of the scarps, as well as plastered over parts of the crater walls and draped across the rim crest (Hawke and Head, 1977). There is clear evidence of leveed channels that connect higher terraces to lower levels ($\sim 30^\circ$ slopes) down to the crater floor apparently carved out by flowing materials originating in higher reservoirs and pools of melted ejecta. The interface between terrace morphology and the flat crater floor is smooth and gradual (e.g. Fig. 12A)

and can be understood in terms of a sequence of events that places the completion of the rim collapse phase prior to the impact melt solidification that overlies the crater floor.

6.3. Rim North (RN)

There is nearly a complete agreement on the differentiation between spectral types using our 'shape matching' technique (Ch. 5.2, Fig. 7) and the Mineral Spectral Parameters (Ch. 5.3, Fig. 8). Given the arbitrary and slightly crude grouping method used to classify spectra in Fig. 8 (inset), we can interpret these two sets in a complementary way, taking the mineralogical description from Fig. 8 and the geographical distribution from Fig. 7. The results show that spectral type 'α', associated with opx-olivine mineralogical spectral attributes (OXO), is found mainly on the less steep or flat terraced areas, whereas 'δ' (pyroxene-olivine, or PXO) is seen on steeper slopes, thus indicating a strong topographical affiliation.

The more detailed analysis and classification carried out through the CNA method (Ch. 5.4, Fig. 11C) reveal a much subtler distribution of spectral types although still dominated by the same three mafic end members: multiphase pyroxene, Ca-poor pyroxene, and olivine. The distribution of these end-members broadly match the first two methods' results with opx representing along with olivine the most common mafic components in the mature materials exposed on the northern slopes. All data indicate strong olivine signatures located on the lower half of the uppermost wall (SN 9887-8) and near the boundary with the crater floor (SN 9914-5). The stronger presence of olivine against the pyroxene phase is also confirmed by the overall Summer Reflectance levels of these sampling points (Figs. 5 and 11A).

The detection of olivine-rich materials across the northern rim and wall terraces has been suggested by several studies (e.g. Chevrel *et al.*, 1991; Le Mouélic and Langevin 2001; Lucey *et al.*, 1991; Sprague *et al.*, 1992; Yamamoto *et al.*, 2010). Pinet *et al.*, (1993) even proposed that olivine might represent the primary mafic component (troctolite) in the northeastern portion of the crater, a conclusion that agrees with our findings. Nevertheless, we feel confident only to confirm the presence of individual (localized) spectral samples with strong olivine absorption characteristics, probably indicating a mono-phase mafic component as mentioned in this chapter, but the more common and much weaker presence of olivine-like spectral features may be explained by the complex and overlapping absorption features of various mafic and glass components (pyroxene, olivine, and Fe-rich impact glass). We propose instead low-Ca pyroxene as the major mafic component across the rim and terraces, related to the probable target materials (e.g. Fig. 2) and similar in composition to feldspathic breccias (Pieters 1982).

6.4. Rim South (RS)

Both the north-south morphologic and compositional asymmetry of the rim regions are well known and clearly shown in Fig. 2. The southern crater rim features less steepen walls and a more complex morphology to the northern one. It also extends further into the crater floor suggesting a complex modification stage where target materials and morphology probably dictated the final shape of the crater. As mentioned in the introduction, the angle of impact (taken as $\ll 90^\circ$) might have had an influence on the mechanisms of target materials removal and ejecta production and distribution. Fig. 2 also shows the strong spectral presence of freshly exposed and/or crystalline materials along the exposed rim terraces as deduced from color-ratio images (e.g. Spudis *et al.*, 1988).

The south rim presents some of the most extreme spectral samples found within the crater: SN 10031-2 have the lowest reflectance values of the whole sampled pool (Fig. 6) while SN 10014 stands out by the apparent absence of a 2 μm absorption feature against SN 10040, in which the feature is strongest.

Fig. 7 clearly illustrates the spectral dichotomy between the northern and southern rims, in particular with the presence of type 'ζ' that is found only on the southern rim. In general, pyroxene rich (or freshly exposed) materials are most strongly represented here and in particular, and uniquely, the more calcium-rich phases. In particular, SN 10040 (but also 10043-47-52) shows relatively strong cpx spectral features. It is problematic if not impossible to quantify the actual pyroxene ratio just from NIR spectral characteristics alone, but, as we noted earlier, cpx absorption features are generally weaker than opx. Consequently, when cpx is present in a mix with other pyroxenes, it reveals itself spectrally only when at concentrations are generally $>3/4$ (cpx/opx)(e.g. Cloutis and Gaffey, 1991).

The CNA, although agreeing on the strong pyroxene signature of the exposed materials, offers again a more detailed interpretation of local spectral variations. Unlike the materials on the northern rim, here the summed reflectance values appear unrelated to the composition of the surveyed surfaces but only to follow the illumination environment of the investigated point.

There are three spectral samples, in particular SN 10014-15 that stand out for showing strong absorptions usually associated with olivine. SN 10014 actually represents the most likely spectral candidate for the rock dunite, with olivine the principle mineral component. This sample may share a similar origin with the north wall olivine-rich materials, possibly as

ejecta originating from the central peaks region. Alternatively, but less likely, it could represent autochthonous materials exposed by gravitational slumping.

Other ‘unusual’ spectral samples are those classified as “glass+pyroxene”, in virtue to their strong and broad absorptions around 1 μm (SN 10023-4, 10039, and 10053-5). One would have expected this type of signature to be much more common within the crater; however, our mineralogical interpretation, as per Table 2, might need revising if we find further evidence of impact glass signature being misunderstood for olivine in darker samples.

6.5. Crater Floor

The crater floor in a complex crater can either be described in terms of the annular ‘moat’ surrounding the central peak structure (Gault *et al.*, 1968) or of the central peaks protruding through the crater floor. Brecciated material probably makes up most of the floor basement composition in all craters but in the TYC-type (Ch. 2.3) this is overlaid by a thick sheet of solidified impact melts (Hawke and Head, 1977) reflecting the stratigraphic sequence through which they lined the transient crater bowl (Gault *et al.*, 1968). Copernicus’ crater floor possesses an overall flat topography along with a rather heterogeneous morphology comprising of large sections of rough terrain with a mottled appearance (suggesting complex sub-melt layer topography). This has been associated with displacement and shearing of slump blocks at depth (Melosh, 1989). **Fig. 12F** shows a clear example of these, often large protuberances mottling the otherwise flat floors. Also note the exposed rock boulders (presumably anorthositic breccias) and fragments on the structure’s flanks. **Fig. 12G** is an image of a crater formed by an impact over a similar geological feature characterized by an asymmetrical distribution of discrete blocks over the crater walls, probably due to varying steepness angles effecting gravitational slumping of loose materials.

Towards the end of the modification stage and terrace formation, the base of the slump block would creep back towards the centre of impact over highly fractured and uneven bedrocks, disrupting in the process the final outward flow of melt materials. Shrinkage of the rapidly cooling surface melt layer over the shocked breccia, associated with localized drainage, would result in the highly hummocky terrain we observe across three quarters of the crater floor (e.g. Fig. 4). This roughness is peculiarly absent in the north-western quarter of Copernicus and can be in part explained by the topography of the impacted area (the north-western rim stands between 300 and 900 m higher than the rest of the crater, thereby mirroring the likely pre-impact topography which might have facilitated a higher reflux of melt materials into the crater floor that submerged most minor protuberances).

6.6. Floor North (FN)

Figs. 7 and 8 track spectral variations identically: the almost totality of spectral types according to the MSP belong to the orthopyroxene-olivine index group with two notable exceptions corresponding to localized spikes in NIR reflectance: SN 9949 (olivine-rich) and SN 9962-3 (cpx-rich). The former might share a similar origin as some of the olivine-rich materials found on the northern terraces, i.e. debris or clasts excavated from depth and emplaced as ejecta from the central peak region, and the latter might represent un-weathered materials excavated by a relatively fresh impact crater (Fig. 5).

The more detailed CNA method offers again a rather more complex representation of the spectral distribution across the plain. For instance, we detected a strong presence of orthopyroxene-rich materials in four distinct locations (i.e. SN 9945-6), probably representing either outcrops or boulders relating to the mineralogical composition of the pre-

impact target area, i.e. highland terra (i.e. noritic anorthosite) with a smaller contribution from the otherwise prevalent impact glasses.

The inferred olivine presence is much smaller than across the northern rim, nevertheless still representing a significant mafic component within the crater floor. SN 9949's strong olivine signature highlighted by the two other investigative methods is not detected as strongly here ("Dcg1", Table 2), although still classified as "mature+ol". However, SN 9954 shows the strongest olivine absorption features of the FN hinting at the considerable potential for the MSP method in detecting subtle spectral variations. The spectral samples 9962-3, associated with relatively freshly excavated materials are here reported as found to be opx-rich (Fig. 8), as in agreement with other studies (Chevrel *et al.*, 1991; Smrekar and Pieters, 1985).

Fig. 12E shows a crater around 340 m in diameter and discussed in some detail in Section 6.1. This may represent the key to the understanding of the geomorphology of the northern crater floor, which appears to be composed of noritic or olivine-noritic materials (e.g. Warell *et al.*, 2004), mostly shocked and brecciated overlaid by a relatively thin (in the order of a few tens of meters) veneer of dark and relatively uniform impact materials (see also Pinet *et al.*, 1992). These impact glasses, which by definition are friable and weakly welded together, would have been weathered and pulverized (i.e. reduced to regolith) relatively quickly within the lifetime of the crater, resulting in the smooth texture observed today (i.e. Fig. 12D).

Larger impacts would have excavated higher-albedo materials and these can be observed across the whole region (Fig. 12G) as 'white' boulders and rocks (probably noritic and/or anorthositic breccias). One of the most intriguing features scattered across the FN are elevated mounds and flat-topped hills (small plateaus, Fig. 12F) featuring flanks peppered with those light, coherent boulders observed in association with larger impacts in the area.

One explanation would be that these plateaus represent the underlying elevated topography,

also draped by impact melts, that has been removed along the flanks, exposing the more coherent materials below. With time, some of these exposed materials have disaggregated and gravitationally collapsed at the foot of the plateaus.

6.7. Floor South (FS)

The crater floor south of the central peaks appears morphologically rather different from the RN. Here the floor is less smooth and it is clustered with boulders and wrinkle-like features (i.e. Fig. 12B). Subsurface shortening and a more pronounced inward collapse of the southern rim has already been proposed here and elsewhere (e.g. Melosh, 1989).

Our spectral models on the whole describe the materials exposed in this area as ‘transitional’ in character, with olivine as the major mafic component (i.e. SN 9986-88) gradually being replaced by pyroxene as we move southwards (SN 10003-4 and SN 10010-11).

The narrow boundary area between the floor and the south rim shows a brief ‘return’ of the spectral signature of olivine (at SN 10012), probably related to the samples 10014-15 inside the southern rim (as discussed in Ch. 6.4), and characterized by some of the strongest monophase absorptions within the crater.

6.8. Peak Complex

It has long been established that central peaks represent deep-seated bedrock (e.g. Schmitt *et al.*, 1967). Hale and Head (1979) classified the Copernicus’ central peaks as ‘Type C, Complex’ (an elongate cluster of ridges, see Ch. 2.3). Cintala *et al.*, (1977) noted that linear central peaks are preferentially developed in the highlands, and concluded that the pre-impact geomorphology plays a key role on the emplacement dynamics of the surfaced rocks. Studies of terrestrial impacts and modelled planetary dynamics of complex crater morphometry (e.g.

Grieve *et al.*, 1981) have found the stratigraphic uplift of central peaks to be in the region of 1/10 of the crater final diameter (about 9 km in the case of Copernicus). Cintala and Grieve (1998) proposed that the central peaks' materials originate from the maximum depth of melting during excavation and represent rocks 'caught' between stress-relieving decompression wave fronts travelling through both the target materials (shock wave front) and the projectile (reflected rarefaction wave) [also Pike, 1980]. Thus, the central peaks of complex craters offer a unique opportunity to access lunar materials from depth.

6.9. Central Peak (CP)

Copernicus' central peaks have been the focus of much remote sensing research since their VIS-NIR spectra were found to display an unusual "broad, multiple band absorption feature centered near 1 μm " and little or no '2 μm ' absorption, a spectral signature broadly comparable to those of lunar dunite/troctolite samples (Pieters 1982).

Subsequent research (e.g. Chevrel *et al.* 1991; Le Mouélic *et al.*, 2001; Lucey *et al.*, 1991; Pieters, 1986; Pieters and Wilhelms, 1985; Salisbury *et al.*, 1987; Sprague *et al.*, 1992; Sunshine and Tomkins, 2001; Yamamoto S. *et al.*, 2010) have confirmed the distinctive spectral signature of the sampled region, in particular of Pk3 (**Figure 13A**).

Both the mineral indexes and 'shape' comparison method broadly agree on the location of olivine-rich outcrops. Indeed, all investigative methods indicate SN 9967-8 and 9978 as the strongest candidates for the detection of troctolite or even dunite. Pieters *et al.*, (1990) estimated an upper limit of about 30% plagioclase for Pk3, a figure that can be supported by our study. Interestingly, both the CNA and the 'shape matching' method highlight samples 9981-3 as equally displaying a strong olivine signature despite their weak overall reflectance levels (see range SN 9977-9984 in Fig. 5).

LROC images offer revealing details on the nature of the central peaks (Fig. 13). Fig. 13A shows Pk3's (also Fig. 4) 'missing' south-western flank, presumably carved out by an impact. The rock texture appears highly fractured and brecciated and rather uniform both in appearance and color. Boulders and smaller debris fractions have gathered throughout million of years at the foot of the mountains as scree and talus. **Fig. 13B** shows an example of the probable travel of loose materials that has been (1) gravitationally transported downslope (2) along terraced grooves and collected at the foot of the slope with larger boulders and rocks coming to rest further down (3).

The high resolution images highlight the sharpness of the boundary between the dark mare-like crater infill and the light-colored mountains (in particular **Figs. 13C, D, and E**). Fig. 13D shows dark, smooth, but also a highly cratered floor against a 'fresh' mountain face. As we rule out a later resurfacing of the central peaks to account for the paucity in crater population, we can speculate that the peaks are composed of highly brecciated and unconsolidated materials (presumably highly shocked and brecciated megaregolith from the deeper crust) which promptly readjust to minor cratering events, much like a gravel heap if hit by a stone. The sharp boundary could be an artefact caused by a gravitationally (later also impact-led) desegregation and collapse of the surfaced peak materials following the modification stage. This mechanism implies a relatively rapid crystallization of the melt sheet within the crater floor as suggested by the partially embayed boundary topographic features as seen in figures 13D and E.

7. CONCLUSIONS

We have analyzed newly acquired NIR multispectral data from the SIR-2 instrument on board of the Chandrayaan-1 lunar mission in order to test the value, consistency, and

interpretative methods within a geological area that has been shown to display a wide range of reflectance spectral behavior. The Copernicus impact occurred on a border area between highland and mare units, a lunar region that had already witnessed a series of major impact events. The underlying stratigraphy is hence both complex and badly constrained.

This study has employed three complementary methods in order to elaborate consistent mineralogical estimates in spite of lacking information for much of the diagnostic sub-one micron spectral region. The first method, as per Fig. 7 and reproduced for comparison as Fig. 11B, maps normalized spectra with similar absorption features ('shape') across the crater interior. This first-order analysis allowed a preliminary differentiation and classification of the entire spectral pool into six main spectral types (α to ζ).

We then applied a numerical spectral ratio method (Table 1) to obtain mineralogical index values offering a qualitative interpretation of the major mafic fractions (Fig. 8). These results were then arbitrarily subdivided into compositional mix types (Fig. 8 inset) and mapped for comparison (Fig. 11C).

Finally, we applied a double normalization method (CNA) developed by the authors aimed at offering a more detailed estimation of the mineralogical species with dominant absorption features. The results are offered both in terms of 'Spectral Type' (Fig. 11D, based on Fig. 10d) and subsequent mineralogical interpretation (Fig. 11E).

We propose that detailed differentiation of mineral species to be achievable within the relatively narrow near-infrared wavelength range using the CNA method, as long as the data are consistent across large sets and locations to allow reliable cross-calibration and comparisons.

The results suggest that the absorption characteristics of olivine to be detectable over several locations across the crater's interior. There is an alternative interpretation though, which associates the broad 1 μm absorption instead to Fe-rich (impact) glass component. This hypothesis can be tested on other impact craters where any presence of olivine in the exposed materials is highly unlikely. In this case, Table's 2 (and Fig. 11E) mineralogical interpretation "mature+ol" would then be reclassified as a glass-rich soil.

Less equivocal and stronger olivine absorption characteristics are found in correspondence to the central peak mountains, but also on the northern crater walls and in one location at the border with the south rim. The general high reflectance characteristics of these samples (Fig. 11A) are also diagnostic of the dominance of the mafic phase olivine in place of pyroxene (still with plagioclase as the probable main silicate fraction).

Strong Ca-poor pyroxene signatures are detected over most of the crater interior but across the southern rim it is progressively replaced by Ca-richer pyroxene phases as we move southwards. The distribution of pyroxenes based on their calcium content helps in differentiating between (mineralogically) less evolved highland materials (opx-dominated, troctolites) and mare-like materials (cpx-dominated, gabbros). The asymmetrical distribution of these two petrologies across the crater supports the hypothesis that the impact occurred on a geologic boundary region (Ch. 2.2).

We do not attempt to add to the various models of the origin of the olivine phase on the lunar surface since this subject has been thoroughly investigated by numerous authors (e.g. Pieters *et al.*, 1984; Pieters and Tompkins, 1999; Pieters and Wilhelms, 1985) and no new element (e.g. a new mineral phase) has been detected in our analysis to allow us to build yet another, and highly speculative, petrogenesis model. We can only remark that if we interpret the

diagnostic absorption characteristics in the near-infrared to provide evidence of widespread olivine components across much of the crater interior, we must consider either a relatively shallow source of noritic olivine (a pluton? a mantle intrusion?) or the consequences of complex mineralogical fractionations of composite target materials.

In our future work we aim to refine our spectral interpretation and comparative derivation of both qualitative and quantitative mineralogical analysis and to develop a database of spectral types, in our case focused on the NIR range as detected by SIR-2 instrument, to be employed as a blueprint for further research in other areas of the Moon and, possibly, beyond.

Acknowledgements:

The project was funded through the Max-Planck Society, Germany and the European Space Agency. We thank the University of Bergen, Norway, for support.

REFERENCES

- Adams J.B., 1974. Visible and near-infrared diffuse reflectance spectra of pyroxene as applied to remote sensing of solid objects in the Solar System. *J. Geophys. Res.* 79, 4829-4836. DOI: 10.1029/JB079i032p04829
- Adams J.B., 1975. Interpretation of visible and near-infrared diffuse reflectance spectra of pyroxenes and other rock forming minerals; In: *Infrared and Raman spectroscopy* (Karr, Jr., Ed.). Academic Press, New York and London, 91-116.
- Ahrens T.J, O'Keefe J.D., 1977. Equations of state and impact-induced shock-wave attenuation on the moon; In: *Impact and explosion cratering.* (eds. D. J. Roddy, R. O. Pepin, R. B. Merrill). Pergamon Press, NY., 639-656.
- Baron R.L., Bilson E., Gold T., Colton R.J., Hapke B., Stegert M.A., 1977. The surface composition of lunar soil grains: A comparison of the results of auger and x-ray photoelectron (ESCA) spectroscopy. *Earth Planet. Sci. Lett.* 37, 263-272.
- Bell P.M., Mao H.K., Rossman G.R., 1975. Absorption spectroscopy of ionic and molecular units in crystals and glasses. In: *Infrared and Raman spectroscopy.* (Karr, Jr., Ed.). Academic Press, New York and London, 13881.
- Bell P.M., Mao H.K., Weeks R.A., 1976. Optical spectra and electron paramagnetic resonance of lunar and synthetic glasses: A study of the effects of controlled atmosphere, composition, and temperature. (abstract). LPSC VII, 2543-2559.
- Bibring J.-P., et al., 2005. Mars surface diversity as revealed by the OMEGA/Mars Express observations, *Science* 307, 1576-1581.
- Bogard D.D., Garrison D.H., Shih C.Y., Nyquist L.E., 1994. ³⁹Ar-⁴⁰Ar dating of two lunar granites: The age of Copernicus. *Geochimica et Cosmochimica Acta*, Vol. 58-No14, 3093-3100.
- Bowker D.E., Hughes J.K., 1971. Lunar Orbiter Photographic Atlas of the Moon, NASA, SP-206.
- Burns R.G., 1970. Mineralogical applications of crystal field theory. Cambridge University Press, Cambridge, UK, 224.
- Burns R.G., 1993. Mineralogical Applications of Crystal Field Theory. 3rd ed. "Cambridge Univ., New York", 551.
- Burns R.G., Vaughan D.J., 1975. Polarised electronic spectra. "In: *Infrared and Raman spectroscopy* (Karr, Jr., Ed.). Academic Press, New York and London, 39-72.
- Cassidy W., Hapke B., 1975. Effects of Darkening Processes on Surfaces of Airless Bodies. *Icarus* 25, 371-383.

- Charette M.P., McCord T.B., Pieters C.M., Adams J.B., 1974. Application of Remote Spectral Reflectance Measurements to Lunar Geology Classification and Determination of Titanium Content of Lunar Soils. *J. Geophys. Res.* Vol. 79, Issue 11, 1605-1613. DOI: 10.1029/JB079i011p01605
- Charette M.P., Adams J.B. 1977. Spectral reflectance of lunar highland rocks. *Lunar Planet. Sci.* VIII, 172 (abstract).
- Chevrel S., Pinet P., Lesbre O., 1991. Copernicus: Comparison and complementarity between telescopic multispectral solid state imaging and reflectance spectra. *Lunar Planet Sci.* XXII, 201 (abstract).
- Cintala M.J., Wood C. A., Head J.W., 1977. The effects of target characteristics on fresh crater morphology: Preliminary results for the moon and Mercury. *Lunar Planet. Sci.* VIII, 3409-3425 (abstract).
- Cintala M.J., Grieve R.A.F., 1998. Scaling impact melting and crater dimensions: Implications for the lunar cratering record. *Meteorit. Planet. Sci.* 33, 889-912.
- Clark R.N., 2009. Detection of Adsorbed water and Hydroxyl on the Moon. *Science*, 326, 562-564.
- Cloutis E.A., Gaffey M.J., 1991. Pyroxene spectroscopy revised: Spectral-compositional correlations and relationship to geothermometry. *J. Geophys. Res.* Vol. 96, NO. E5, 22,809-22,826. DOI: 10.1029/91JE02512
- De Hon R.A., 1979. Thickness of western mare basalts. *Lunar Planet. Sci* X, 2935-2955 (abstract).
- De Hon R.A., 1980. The Imbrium Basin: A structural model. Conference on Multi-Ring Basins: Formation and Evolution. LPI - Contribution 414, 15.
- Dence M.R., 1968. Shock zoning at Canadian craters: Petrography and structural implications. In: *Shock Metamorphism of Natural Materials* (B. M. French and N. M. Short, eds.), "Mono Book Corp., Baltimore, 169-184.
- Dence M.R., 1971. Impact melts. *J. Geophys. Res.* 76, 5552-5565. DOI: 10.1029/JB076i023p05552
- Denevi B.W., Lucey P.G., Sherman S.B., 2008. Radiative transfer modelling of near-infrared spectra of lunar mare soils: Theory and measurements. *J. Geophys. Res.* 113, E02003. DOI: 10.1029/2007JE002929
- Durda D., Greenberg R., Jedicke R., 1998. Collisional Models and Scaling Laws: A new Interpretation of the Shape of the Main-belt Asteroid Distribution. *Icarus* 135, 431-440.
- Eggleton R.E., 1964. Preliminary geology of the Rhiphaeus Quadrangle of the moon and definition of the Fra Mauro Formation. *Astrogeol. Studies, Ann. Prog. Rept.*, August 1962-July 1963. Pt. A, U.S. Geol. Survey open-file Rept., 46-63.

- Eliason E., Isbell C., Lee E., Becker T., Gaddis L., McEwen A. and Robinson M., 1999. Mission to the Moon: The Clementine UVVIS Global Lunar Mosaic. PDS Volumes USA_NASA_PDS_CL_4001 through 4078. U.S. Geological Survey.
- Gault D.E., Quaide W.L., Oberbeck V.R., 1968. Shock Metamorphism of natural materials. In: B.M. French, N.M. Short (eds). Mono Book Corp., Baltimore, 87-99.
- Gault D.E., Hörz F., Brownlee D.E., Hartung J.B., 1974. Mixing of the lunar regolith. *Lunar Planet. Sci.* V, 2365-2386 (abstract).
- Gault D.E., Guest J.E., Murray J.B., Dzurisin D., Malin M.C., 1975. Some comparisons of impact craters on Mercury and the Moon. *J. Geophys. Res.* 80, 17, 2444-2460. DOI: 10.1029/JB080i017p02444
- Gillis J.J., Jolliff B.L., 1999. Lateral and vertical heterogeneity of thorium in the Procellarum KREEP terrane: As reflected in the ejecta deposits of Post-Imbrium craters. Workshop on New Views of the Moon II, LPI, 8055.pdf.
- Grieve R.A.F., 1987. Terrestrial impact structures. *Annu. Rev. Earth Planet. Sci.* 15, 245-270.
- Grieve R.A.F., Dence M.R., Robertson P.B., 1977. Cratering process: As interpreted from the occurrence of impact melts. In: *Impact and Explosion Cratering: Planetary and Terrestrial Implications*. (D. J. Roddy, R. O. Pepin, and R. B. Merrill, eds). Pergamon, NY, 791-814.
- Grieve R.A.F., Robertson P.B., Dence M.R., 1981. Constraints on the formation of ring impact structures, based on terrestrial data. "In: *Multi-Ring Basins: Formation and evolution*, Proc. Lunar Planet. Sci. 12A (P. H. Schultz and R. B. Merrill, eds.)". Pergamon Press, 37-57.
- Grieve R.A.F., Cintala M.J., 1982. A method for estimating the initial impact conditions of terrestrial cratering events, exemplified by its application to Brent crater, Ontario. *Lunar Planet. Sci.* XII, 1607-1621 (abstract).
- Grieve R.A.F., Cintala M.J., 1992. An analysis of differential impact melt-crater scaling and implications for the terrestrial impact record. *Meteorit. Planet. Sci.* 27, 526-538.
- Hale W.S., Head J.W., 1979. Central peaks in lunar craters: Morphology and morphometry. *Lunar Planet. Sci.* X, 2623-2633 (abstract).
- Hapke B., 1973. Darkening of silicate rock powders by solar wind sputtering. *The Moon* 7, 342-355.
- Hapke B., Cassidy W., Wells E., 1975. Effects of vapor-phase deposition processes on the optical, chemical and magnetic properties of the lunar regolith. *The Moon* 13, 339-353.
- Haskin L., Gillis J., Korotev R., Jolliff B., 2000. The materials of the lunar Procellarum KREEP Terrane: A synthesis of data from geomorphological mapping, remote sensing, and sample analysis. *J. Geophys. Res.*, 108, E8. DOI: 10.1029/1999JE001128

- Hawke B.R., Head J.W., 1977. Impact melt in lunar crater interiors. *Lunar Planet. Sci.* VIII, 415-417 (abstract).
- Head J.W., 1977. Regional distribution of Imbrium basin deposits: Relationship to pre-Imbrian topography and mode of emplacement. "Interdisciplinary Studies by the Imbrium Consortium 2, Lunar Science Institute Contr.", 268D, 120-125.
- Hess P.C., 1994. Petrogenesis of lunar troctolites. *J. Geophys. Res.*, Vol. 99, NO. E9, 19,083-19,093. DOI: 10.1029/94JE01868
- Housley R.M., Grant R.W., Paton N.E., 1973. Origin and characteristics of excess Fe metal in lunar glass welded aggregates. *Lunar Planet. Sci.* III, 2737-2749 (abstract).
- Housley R.M., Grant R.W., 1975. ESCA Studies of Lunar Surface Chemistry. *Proc. Lunar Planet. Lunar Planet. Sci.* VI, 3269-3275 (abstract).
- Housley R.M., Grant R.W., 1977. An XPS (ESCA) Study of Lunar Alteration Profiles. *Lunar Planet. Sci.* VIII, 3885-3899 (abstract).
- Hunt G.R., Salisbury J.W., 1970. Visible and near-infrared spectra of minerals and rocks. I. Silicate minerals. *Mod. Geology* 1, 283-300.
- Isaacson P.J., Pieters C.M., 2010. Deconvolution of lunar olivine reflectance spectra: Implications for remote compositional assessment. *Icarus* 210, 8-13.
- Janesick J., 2001. Scientific Charge-Coupled Devices (SPIE Press Monograph Vol. PM83). SPIE Publications; 1st edition (January 1)
- James C.L., Letsinger S.L., Basu A., Wentworth S.J., McKay D.S., 2002. Size distribution of FeO Globules in Lunar Agglutinitic Glass. *Lunar Planet. Sci.* XXIV, 1827 (abstract).
- Jolliff B., Gillis J., Haskin L., Korotev R., Wieczorek M., 2000. Major lunar crustal terranes: surface expressions and crust-mantle origins. *J. Geophys. Res.* , 105, E2, DOI: 0.1029/1999JE001103
- Keller L.P., Wentworth S.J., McKay D.S., 1998. Space Weathering: Reflectance Spectroscopy and TEM Analysis of Individual Lunar Soil Grains. *Lunar Planet. Sci.* XX, 1762 (abstract).
- Keller L.P., Clemett S.J., 2001. Formation of nanophase iron in the lunar regolith. *Lunar Planet. Sci.* XXXII, 2097 (abstract).
- Lawrence D.J., Feldman W.C., Barraclough B.L., Binder A.B., Elphic R.C., Maurice S., Thomsen D.R., 1998. Global Elemental Maps of the Moon: The Lunar Prospector Gamma-Ray Spectrometer. *Science*, Vol. 281, Iss. 5382, p. 1484
- Le Mouélic S., Langevin Y., 2001. The olivine at the lunar crater Copernicus as seen by Clementine NIR data. *Planetary and Space Science* 49, 65-70.

Longhi J., 1977. Magma oceanography: 2. Chemical evolution and crustal formation. *Lunar Planet. Sci.* XIII, 601-621 (abstract).

Longhi J., 1981. Modelling equilibrium partial melting: Implications for early lunar differentiation. *Lunar Planet. Sci.* XXII, 625-627 (abstract).

Lucey P.G., Blewett D.T., Hawke B.R., 1998. Mapping the FeO and TiO₂ content of the lunar surface with multispectral imagery. *J. Geophys. Res.* 103(E2), 3679-3700. DOI: 10.1029/97JE03019

Lucey P.G., Hawke B.R., Horton K., 1991. The distribution of olivine in the crater Copernicus. *Geophys Res. Lett.* 18, 2133-2136.

Mall U., Banaszkiwicz M., Brønstad K., McKenna-Lawlor S., Nathues A., Søråas F., Vilenius E., Ullaland K., 2009. Near Infrared Spectrometer SIR-2 on Chandrayaan-1. *Current Sci.* 96, 486-491.

Mall U., Korokhin V., Shkuratov Yu., 2010. Photometric investigations using the SIR-2 data of the Chandrayaan-1 mission. *Lunar Planet. Sci.* XXXII, 1616 (abstract).

McCord T.B., Charette M., Johnson T., Lebofsky L., Pieters C., Adams J., 1972. Lunar spectral types. *J. Geophys. Res.* 77(8), 1349-1359. DOI: 10.1029/JB077i008p01349

McCord T.B., Adams J.B., 1973. Progress in remote optical analysis of lunar surface composition. *Moon* 7, 453-474.

McGetchin T.R., Settle M., Head J.W., 1973. Radial thickness variations in impact crater ejecta: Implications for basin deposits. *Earth Planet. Sci. Lett.* 20, 226-236.

McKay D., Heiken G., Basu A., Blanford G., 1991. The Lunar Regolith. *Lunar Sourcebook*. "Heiken, G.H., Vaniman, D.T., and French, B.M., Eds.,". New York: Cambridge Univ. Press, Chap. 7, pp. 285-356.

Melosh H.J., 1989. *Impact Cratering - A Geological Process*. Oxford Monographs on Geology and Geophysics #11. Oxford University Press, NY and Clarendon Press, Oxford.

Morris R.V., 1980. Origins and size distribution of metallic iron particles in the lunar regolith. *Lunar Planet. Sci.* XI, 1697-1712 (abstract).

Morris A.R., Head J.W., Margot J.-L., Campbell D.B., 2009. Impact melt distribution and emplacement on Tycho: a new look at an old question. *Lunar Planet. Sci.* XXXI, 1828 (abstract).

Neukum G., Ivanov B.A., Hartmann W.K., 2001. Cratering Records in the Inner Solar System in Relation to the Lunar Reference System. *Chronology and Evolution of Mars*. 96, 55-86.

Nozette S., et al., 1994. The Clementine Mission to the Moon: Scientific Overview. *Science* Vol. 266, 1835-1839.

Oberbeck V.R., Quaide W.L., Mahan M., Paulson J., 1973. Monte Carlo calculations of lunar regolith, thickness, and distribution. *Icarus* 19, 87-107.

O'Keefe J.D., Ahrens T.J., 1982. Cometary and meteorite swarm impact on planetary surfaces. *J. Geophys. Res.* 87, 6668-6680. DOI: 10.1029/JB087iB08p06668

O'Keefe J.D., Ahrens T.J., 1994. Impact-induced melting of planetary surfaces. In: Large Meteorite Impacts and Planetary Evolution, "eds. B.O. Dressler, R. A. F. Grieve and V. L. Sharpton, Boulder, Colorado, USA", 103-109.

Pelkey S.M., et al., 2007. CRISM multispectral summary products: Parameterizing mineral diversity on Mars from reflectance. *J. Geophys. Res.* Vol. 112, NO. E08S14, 43101. DOI: 10.1029/2006JE002831

Pieters C.M., 1982. Copernicus crater central peak - Lunar mountain of unique composition. *Science* Vol. 215, 59-61.

Pieters C.M., 1986. Composition of the Lunar Highland Crust From Near-Infrared Spectroscopy. *Reviews of Geophysics.* Vol. 24, NO. 3, 557-578.

Pieters C.M., Wilhelms D.E., Paquette R., 1984. Stratigraphy at Copernicus and the Source of Olivine in the Central Peak. *Lunar Planet. Sci.* XV, 643-644 (abstract).

Pieters C.M., Adams J., Mougini-Mark P., Zisk S., Smith M., Head J., and McCord T. 1985. The nature of crater rays: the Copernicus example. *J. Geophys. Res.* 90, B14, 12393-12413. DOI: 10.1029/JB090iB14p12393

Pieters C.M., Wilhelms D.E., 1985. Origin of olivine at Copernicus. *Lunar Planet. Sci.* XV (abstract). *J. Geophys. Res. Supplement*, Vol. 90, p.C415-C420.

Pieters C.M., Pratt S.F., Sunshine J.M., 1990. Petrology of the Olivine Mountains at Copernicus. *Lunar Planet. Sci.* XXI, 962 (abstract).

Pieters C.M., Staid M.I., Fisher E.M., Tompkins S., He G., 1994. A sharper view of impact craters from Clementine data. *Science* 266-5192, 1844-1848.

Pieters C.M., Tompkins S., 1999. The Distribution of Lunar Olivine/Troctolite Outcrops: Mineralogical Evidence for Mantle Overturn? *Lunar Planet. Sci.* XXX, 1286.pdf (abstract).

Pieters C.M., Taylor L.A., McKay D.S., Wentworth S., Morris R.V., Keller L.P., 2000. Spectral characterisation of lunar mare soils. *Lunar Planet. Sci.* XXII, 1865 (abstract).

Pieters C.M., et al., 2009. Character and spatial distribution of OH/H₂O on the surface of the Moon seen by M3 on Chandrayaan-1. *Science* 326, 568-572.

Pike R.J., 1974. Ejecta from large craters on the Moon: Comments on the geometric model of McGetchin et al. *Earth Planet. Sci. Lett.* 23, 265-274.

- Pike R.J., 1980. Size-dependence in the shape of fresh craters on the Moon. In: Impact and explosion cratering. (D. J. Roddy, R. O. Pepin, and R. B. Merrill, eds). Pergamon, NY, pp. 489-509.
- Pinet P.C., Chevrel S., Martin P., 1992. Detailed spectro-mixing analysis of Copernicus Crater from high resolution visible-near infrared imaging data. *Lunar Planet. Sci.* XXIII, 1075 (abstract).
- Pinet P.C., Chevrel S.D., Martin P., 1993. Copernicus: A regional probe of the lunar interior. *Science* 260, 797-801.
- Quaide W.L., Gault D.E., Schmidt R.A., 1965. Gravitative effects on lunar impact structures. *Ann. N.Y. Acad. Sci.* 123, 563-572.
- Rode O., Ivanov B.A., Nazarov M. A., 1979. Atlas of Photomicrographs of the Surface Structures of the Lunar Regolith Particles. Praha: Academia.
- Salisbury J.W., Hapke B., Eastes J.W., 1987, Usefulness of weak bands in mid-infrared remote sensing of particulate planetary surfaces. *J. Geophys. Res.* 92(B1), 702-710. DOI: 10.1029/JB092iB01p00702
- Schmitt H.H., Transk N.J., Shoemaker E.M., 1967. U.S. Geol. Surv. Misc. I-515 (LAC-58).
- Schmidt R.M., Housen K.R., 1987. Some recent advances in the scaling of impact and explosion cratering. *Int. J. Impact Engin.* 5, 543-560.
- Schnetzler C.C., Philpotts J.A. 1971. Trace element studies of lunar samples. *Meteorit. Planet. Sci.* Vol. 6, p. 310.
- Schuraytz B.C., Sharpton V., Marín L.E., 1994. Petrology of impact-melt rocks at the Chicxulub multiring basin, Yucatán, Mexico. *Geology* 22, 868-872.
- Shoemaker E.M., 1962. Interpretation of lunar craters. In Z. Kopal (Ed.), *Physics and Astronomy of the Moon*. Academic Press, New York and London, 238-359.
- Simonds C.H., Warner J.L., Phinney W.C., McGee P.E., 1976. Thermal model for impact breccia lithification: Manicouagan and the Moon. *Lunar Planet. Sci.* VII, 2509-2528 (abstract).
- Simonds C.H., Floran R.J., McGee P.E., Phinney W.C., Warner J.L. 1978. Petrogenesis of melt rocks, Manicouagan impact structure, Quebec. *J. Geophys. Res.* 83, pp. 2773-2788. DOI: 10.1029/JB083iB06p02773
- Singer R.B., 1981. Near-infrared spectral reflectance of mineral mixtures: Systematic combinations of pyroxenes, olivine, and iron oxides. *J. Geophys. Res.* 86, 7967-7982. DOI: 10.1029/JB086iB09p07967
- Smrekar S., Pieters C.M., 1985. Near-Infrared Spectroscopy of Probable Impact melt from Three Large Lunar Highland Craters. *Icarus* 63, 442-452.

- Snyder G.A., Taylor L.A., Neil C.R. 1992. A chemical model for generating the sources of mare basalts: Combined equilibrium and fractional crystallisation of the lunar magmasphere. *Geochim Cosmochim Acta* 56:3809-3823.
- Sprague A.L., Witteborn F.C., Kozlowski R.W., Cruikshank D.P., Bartholomew M.J., Graps A.L., 1992. The Moon: Mid-Infrared (7.5- to 11.4- μm) Spectroscopy of Selected Regions. *Icarus* 100, 73-84.
- Spudis P.D., 1993. *The Geology of Multi-Ring Impact Basins - The Moon and Other Planets*. Cambridge University Press, Cambridge, UK.
- Spudis P.D., Hawke B.R., Lucey P.G., 1988. Materials and formation of the Imbrium Basin. *Lunar Planet. Sci. XVIII*, 155-168 (abstract).
- Stöffler D., 1984. Glasses formed by hypervelocity impact. *J. Non-Crystall. Solids* 67, 465-502.
- Stöffler D., Knoll H-D., Marvin U. B. Warren P. W. 1980. Recommended classification and nomenclature of lunar highland rocks – A committee report. In *Proceedings of the Conference on the Lunar Highlands Crust* (eds. J. J. Papike and R. B. Merrill), pp. 51-70. Pergamon Press, New York, New York, USA.
- Stöffler D., Langenhorst F., 1994. Shock metamorphism of quartz in nature and experiment: I. Basic observation and theory. *Meteorit. Planet. Sci.* 29, 155-181.
- Stöffler D., Ryder G., 2001. Stratigraphy and Isotope Ages of Lunar Geologic Units: Chronological Standard for the Inner Solar System. *Space Sci. Rev.* 96, 9-54.
- Sunshine, J., Pieters C., and Pratt S. 1990, Deconvolution of Mineral Absorption Bands: An Improved Approach, *J. Geophys. Res.*, 95(B5), 6955-6966. DOI: 0.1029/JB095iB05p06955
- Sunshine J.M., Tomkins S., 2001. Yet another new look at Copernicus: Projecting telescopic spectra onto Clementine multispectral images through spectral mixture analysis. *Lunar Planet. Sci. XXIII*, 1324 (abstract).
- Sunshine J.M., et al., 2009. Temporal and spatial variability of lunar hydration as observed by the Deep Impact spacecraft. *Science* 326, 565-568.
- Taylor S.R., 1975. *Lunar Science: A post Apollo view*. Pergamon Press, NY, 372.
- Taylor S.R., 1982. *Planetary Science: A lunar prospective*. Lunar and Planetary Institute, Houston, 481.
- Taylor S.R., Jakes P. 1974. The geochemical evolution of the Moon. *Lunar Planet. Sci. V*, 1287-1305 (abstract).
- Taylor G.F., Warren P., Ryder G., Delano J., Pieters C., Lofgren G., 1991. Lunar surface processes. In: *Lunar Sourcebook: a User's guide to the Moon* (G. H. Heiken, D. T. Vaniman, and B. M. French, eds.). Cambridge Univ., New York, 183-284.

Warell J., Sprague A.L., Emery J., Long A., 2004. Moon: First Spectra from 0.7 to 5.5 μm . *Lunar Planet. Sci.* XXXV, 1624 (abstract).

Wells E., Hapke B., 1977. Lunar soil: Iron and titanium bands in the glass fraction. *Science* 195, 977-979.

Wentworth S.J., Keller L.P., McKay D.S., Morris R.V., 1999. Space Weathering on the Moon: Patina on Apollo 17 samples 75075 and 76015. *Meteorit. Planet. Sci.* 34, 593-603.

Wilcox B.B., Lucey P.G., Gillis J.J., 2005. Mapping iron on the lunar mare: An improved approach. *J. Geophys. Res.* 110, E11001. DOI: 10.1029/2005JE002512.

Wilhelms D.E., 1970. Summary of lunar stratigraphy - Telescopic observations. U.S. Geol. Survey Prof. Paper. 599-F, 47.

Wilhelms D.E., Davis D.E. 1971. Two former faces of the Moon. *Icarus* 15, 368-372.

Wood C.A., Andersson L., 1978. New morphometric data for fresh lunar craters. *Icarus* 20; 503-506.

Yamamoto S., et al., 2010. Global distribution of olivine exposures on the Moon revealed by SELENE Spectral Profiler. *Lunar Planet. Sci.* XXXII, 1646 (abstract).

ACCEPTED MANUSCRIPT

FIGURES CAPTIONS

- Figure 1. Color inset shows the Moon as it would have looked at the end of the Imbrian Period. Adapted from Wilhelm and Davis, 1971.
- Figure 2. Copernicus quadrant map, constructed from Lunar Chart LAC 58, Orbiter images, Clementine derived FeO wt% map, and Clementine UVVIS Ratio Images.
- Figure 3. Near-Infrared typical spectra of key mineral components of lunar materials, in particular the anorthosite suite of highland minerals. Modified after Charette and Adams, 1977.
- Figure 4. Panoramic image of Copernicus crater, looking north. Orbiter II-162H3.
- Figure 5. Summed Reflectance (SR) of the Copernicus region. Base map is the Lunar Orbiter image 5151_med photo with superimposed a Clementine False Color map. Reflectance curves from SIR-2 NIR data set, each group relating to a specific geographical region.
- Figure 6. SIR-2 NIR spectra of Copernicus' interior (color coded as: black = crater floor; red = crater rim; green = central peak area): *a*) all 174 spectra; *b*) outstanding spectra (dots representing actual data points); *c*) same as *b*) but normalized to zero reflectance; *d*) chosen representative spectral types.
- Figure 7. Geographical distribution across Copernicus crater of spectral groups as per Fig. 6. Values at the bottom represent percentage weight for each type.
- Figure 8. Mineral Spectral Parameters (MSP). Scatter distribution of pyroxenes and olivine indexes as derived from parameters in Table 1. For ease of identification, clouds

enclose most samples according to their geographical location within the crater. Inset at bottom right represents an arbitrary classification of spectral types (see also Table 2 and Fig. 11C) where: O = olivine; PXO = pyroxene-olivine; OXO = orthopyroxene-olivine; PX = pyroxene; CX = clinopyroxene.

Figure 9a-c. Comparative Normalization Analysis (CNA) method. Step 1: *a*) spectrum SN 9978 taken as example; *b*) the 11 waveband centers chosen to represent mineralogical diagnostic absorption features; *c*) same spectrum as *a*) but showing only the sampled wavecentres reflectance values.

Figure 10a-d. Comparative Normalization Analysis (CNA) method. Step 2: *a*) all 174 spectra derived as in Fig. 9 and mapped across Copernicus' interior; *b*) as *a*) but normalized; *c*) normalized reflectance level as from *b*); *d*) further grouping and averaging down to seven key absorption ranges.

Figure 11. Spectral classifications mapped for comparison: A) Summed Reflectance; B) 'Shape' class from Fig. 7; C) MSP from Fig. 8; D) CNA derived from Fig. 10d; E) mineralogical interpretation of spectral absorption features based on the CNA method.

Figure 12a-g. Images selected and extracted from image M102293451LE (NACL, 251, EDR). Lunar Reconnaissance Orbiter Camera (NASA/GSFC/Arizona State University, LRO lunar mission). Descriptions in text.

Figure 13a-e. Images selected and extracted from image M102293451LE (NACL, 251, EDR), M114084316LE (NACL, 1946, EDR) and M111728277RC (NACR, 1599, EDR). Lunar Reconnaissance Orbiter Camera (NASA/GSFC/Arizona State University, LRO lunar mission). Descriptions in text.

TABLES CAPTIONS

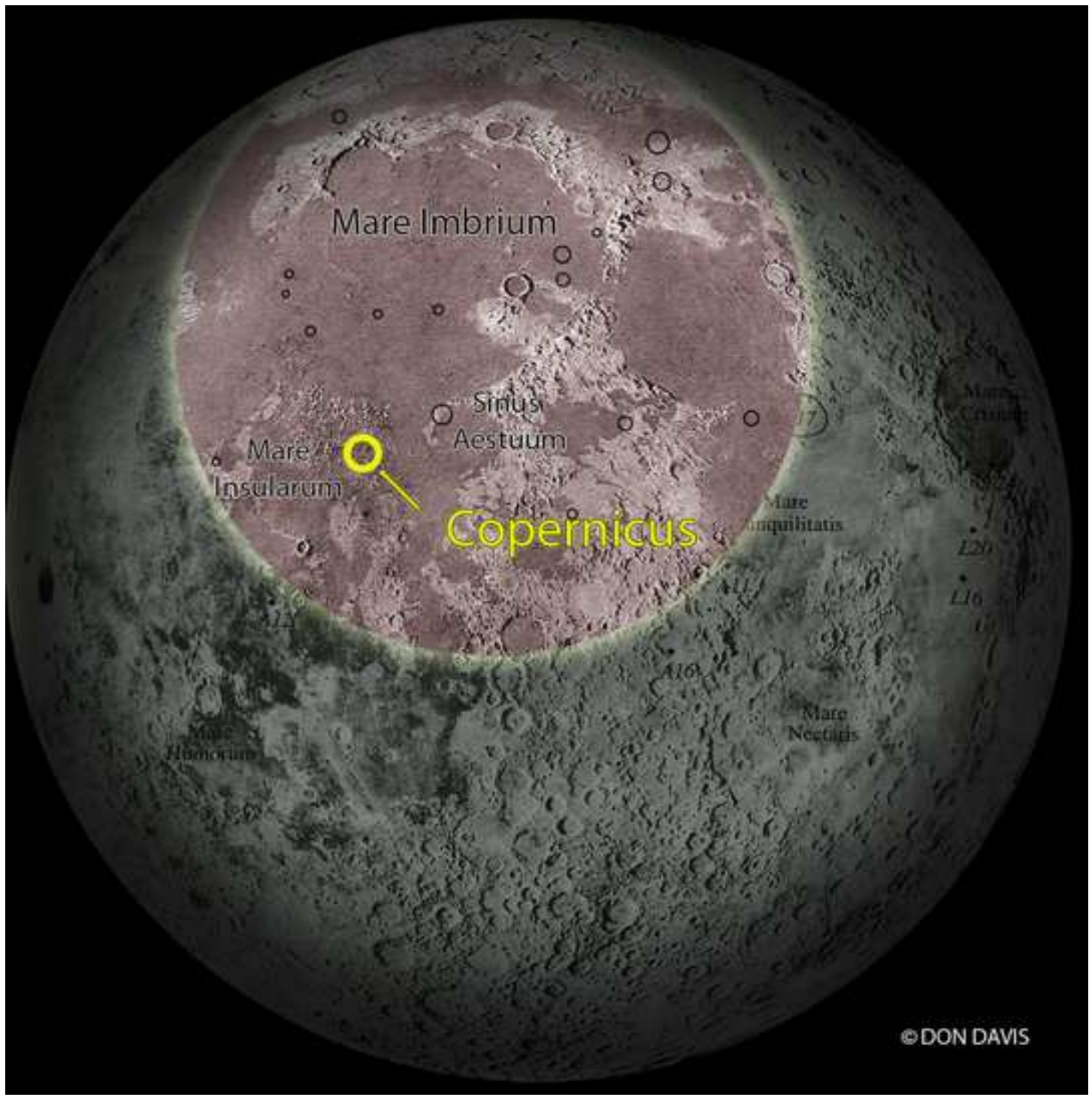
Table 1. Mineral Spectral Parameters (MSP). Adapted from CRISM Spectral Parameter Products (Pelkey *et al.*, 2007) to SIR-2 band centers.

Table 2. Table gathering all spectral classification results as: SN (Spectral Number, from North to South, color coded to delineate morphological boundaries); Fig. 7 spectral 'Shape'; Fig. 8, Mineral Spectral Parameters (MSP); Spectral Type (CNA); Mineralogical Interpretation, mostly derived from CNA method.

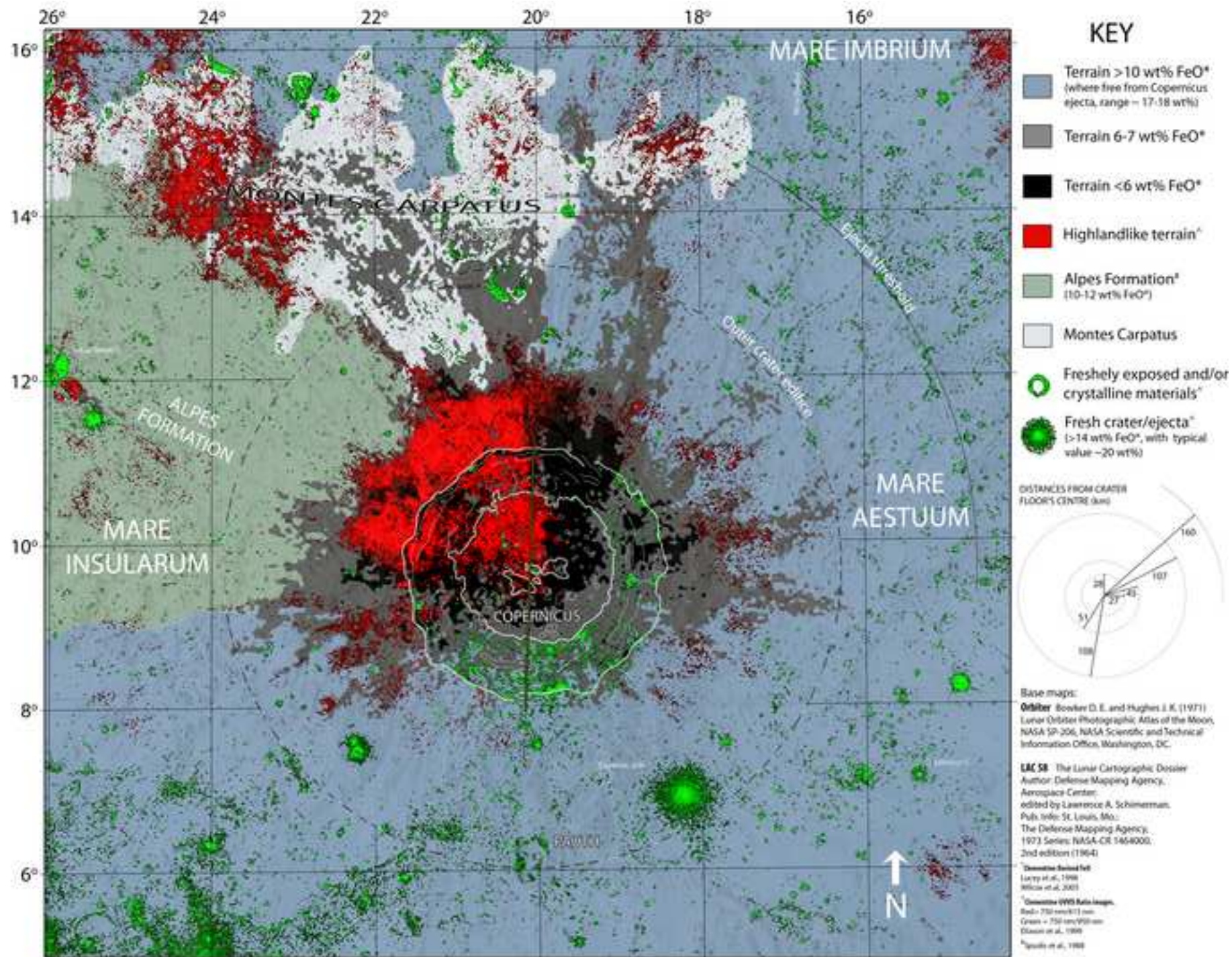
ACCEPTED MANUSCRIPT

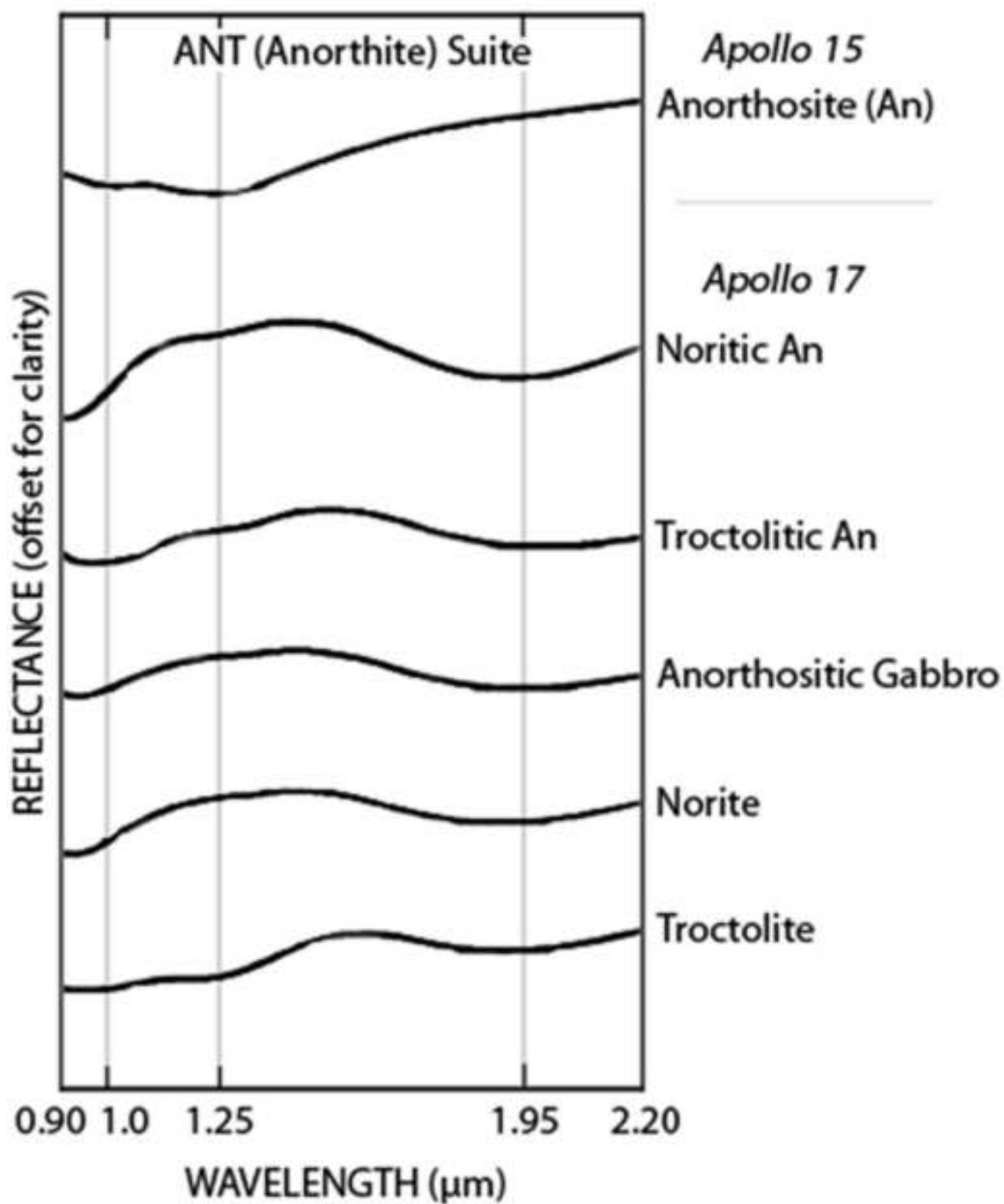
- >We present an in-depth study of Copernicus crater.
- >First publication based on new NIR data from the SIR-2 mission to the Moon.
- >New NIR spectral classification of surface materials within the crater.
- >Highly detailed mapping of spectrally-prominent mineral species.

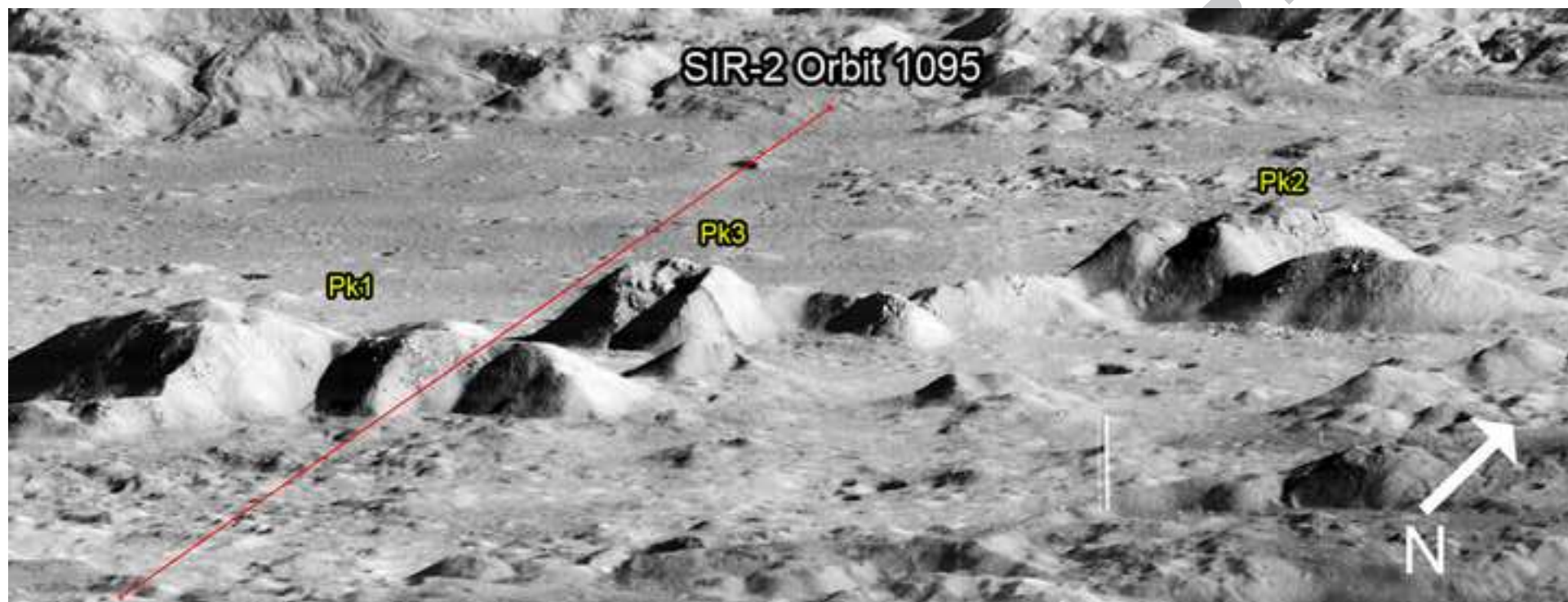
ACCEPTED MANUSCRIPT

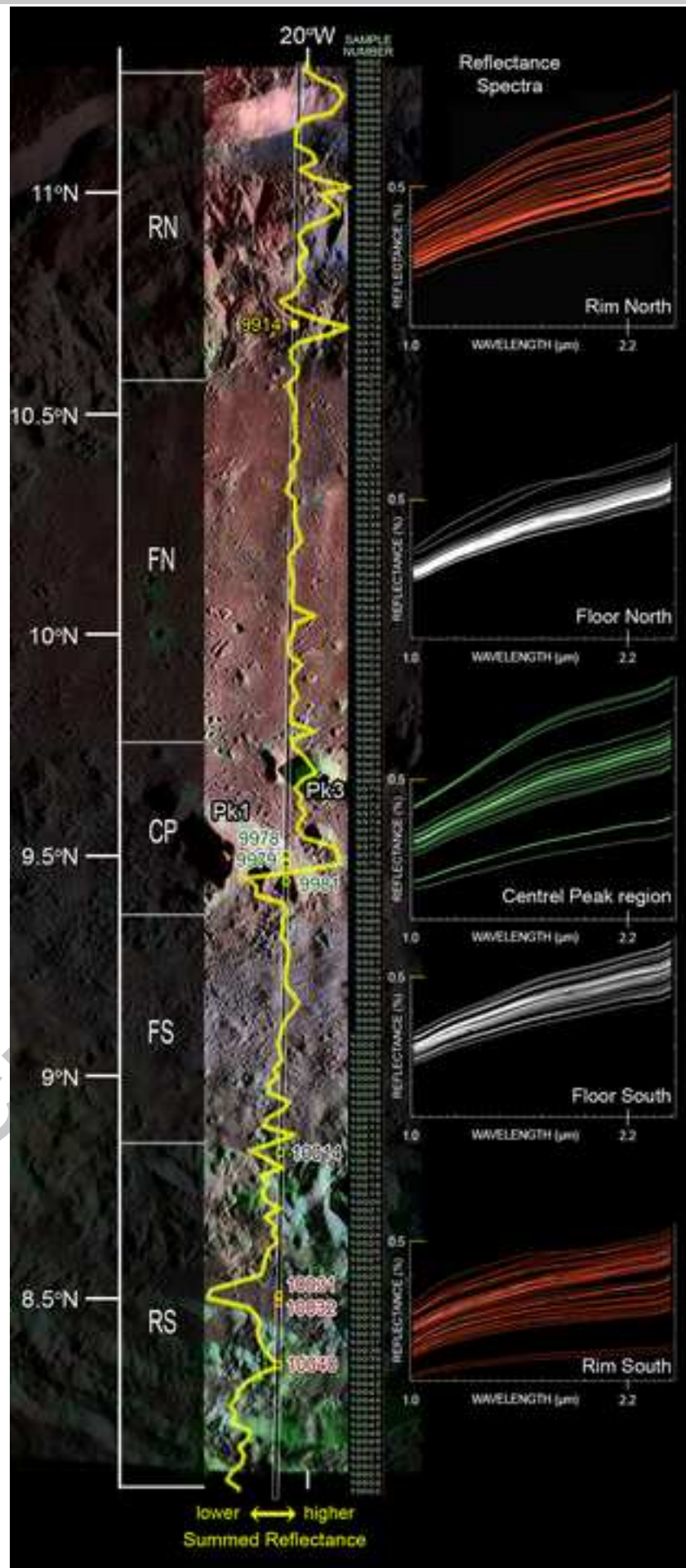


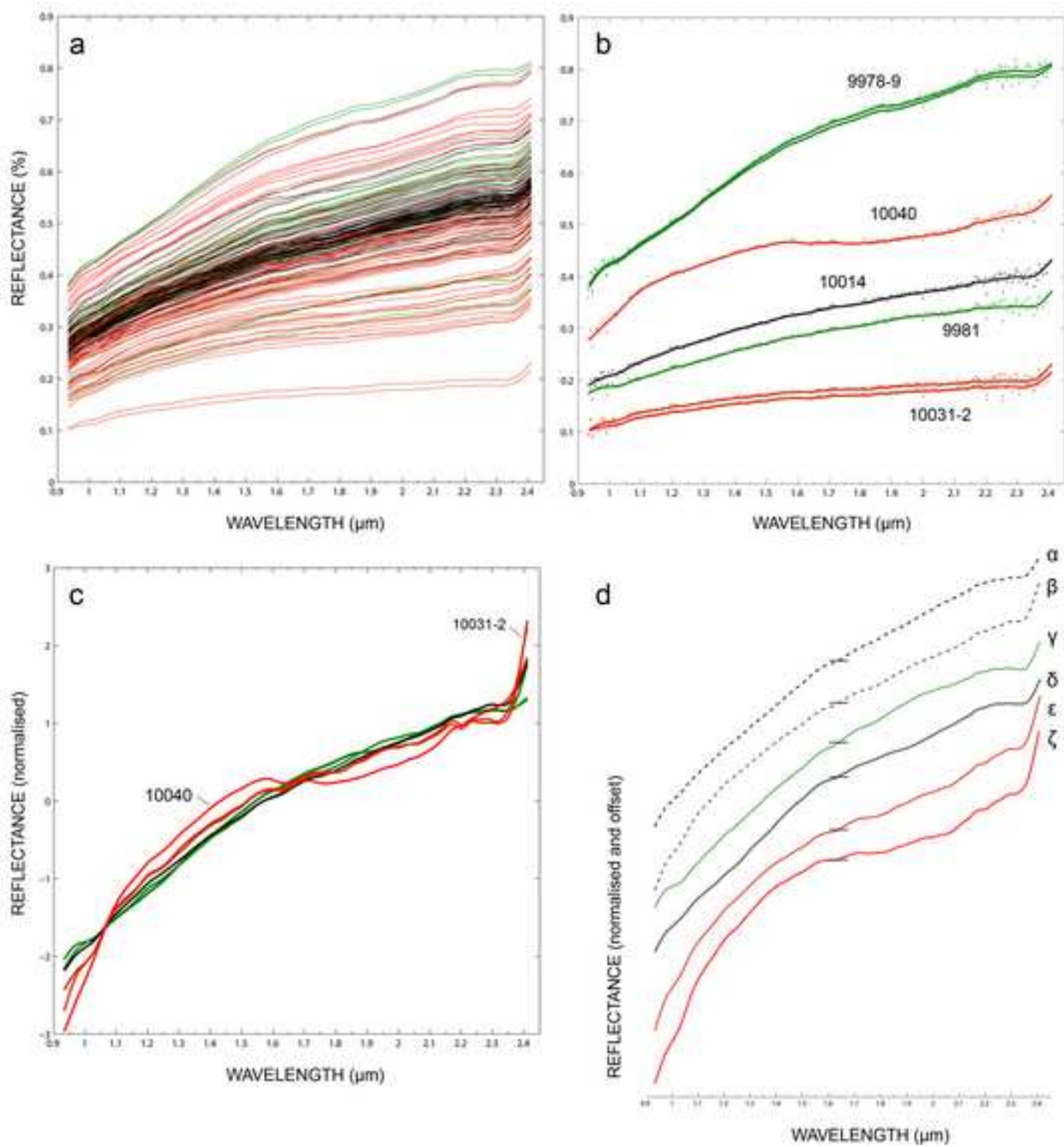
Figure_2

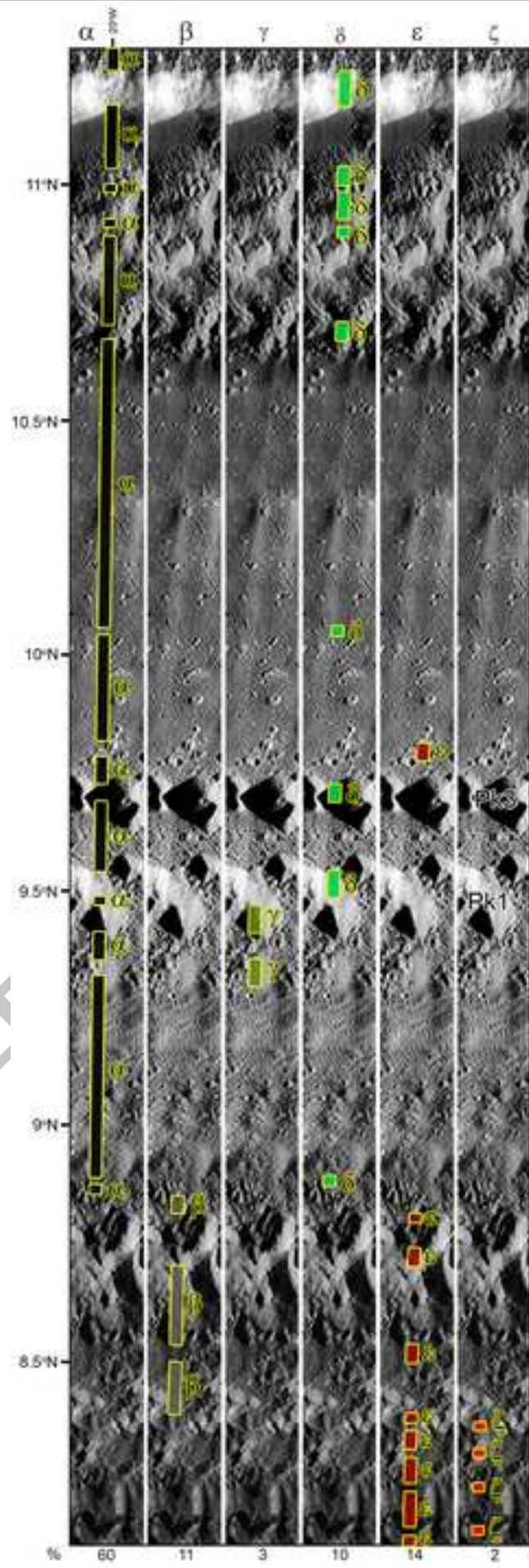






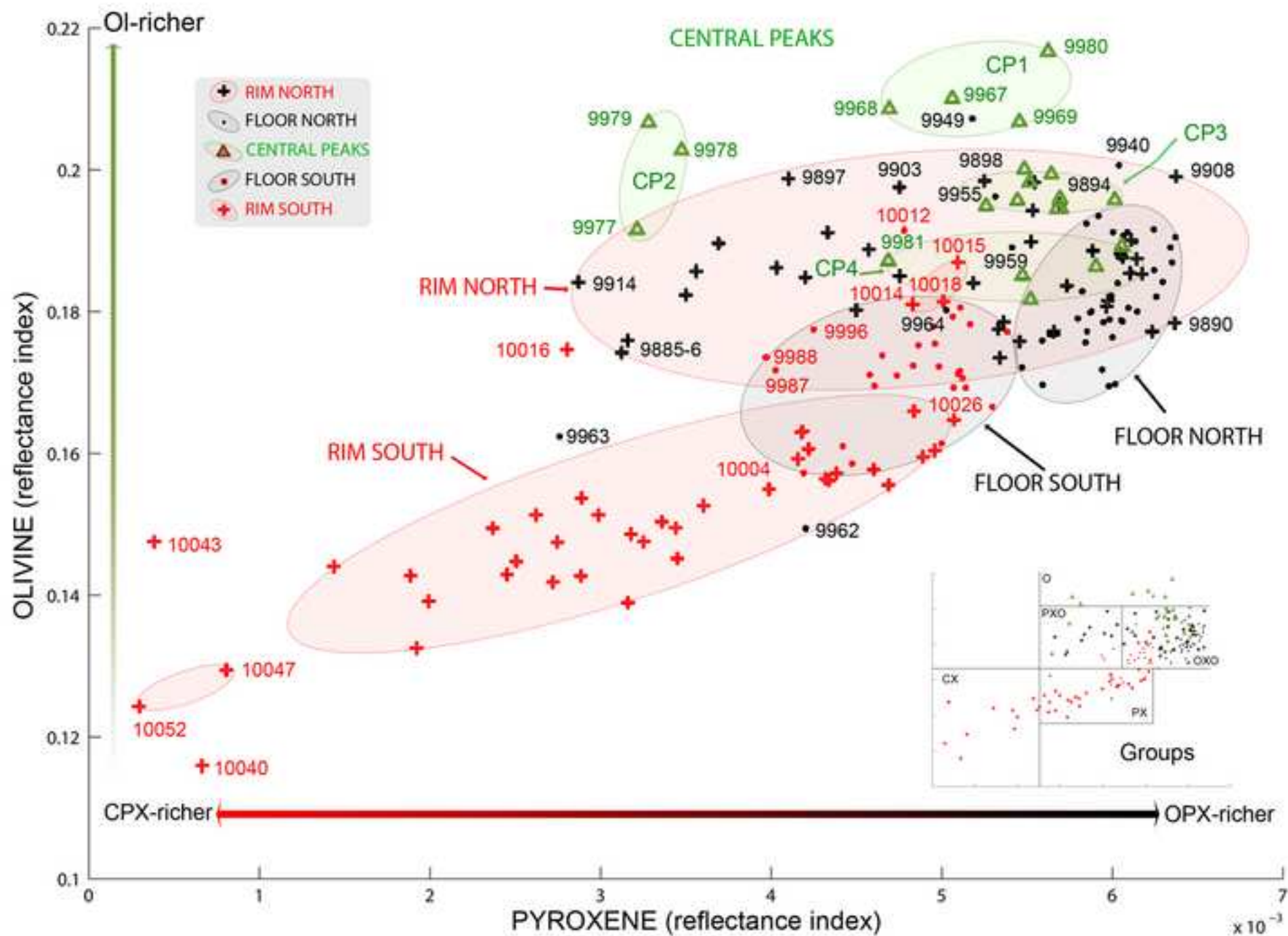


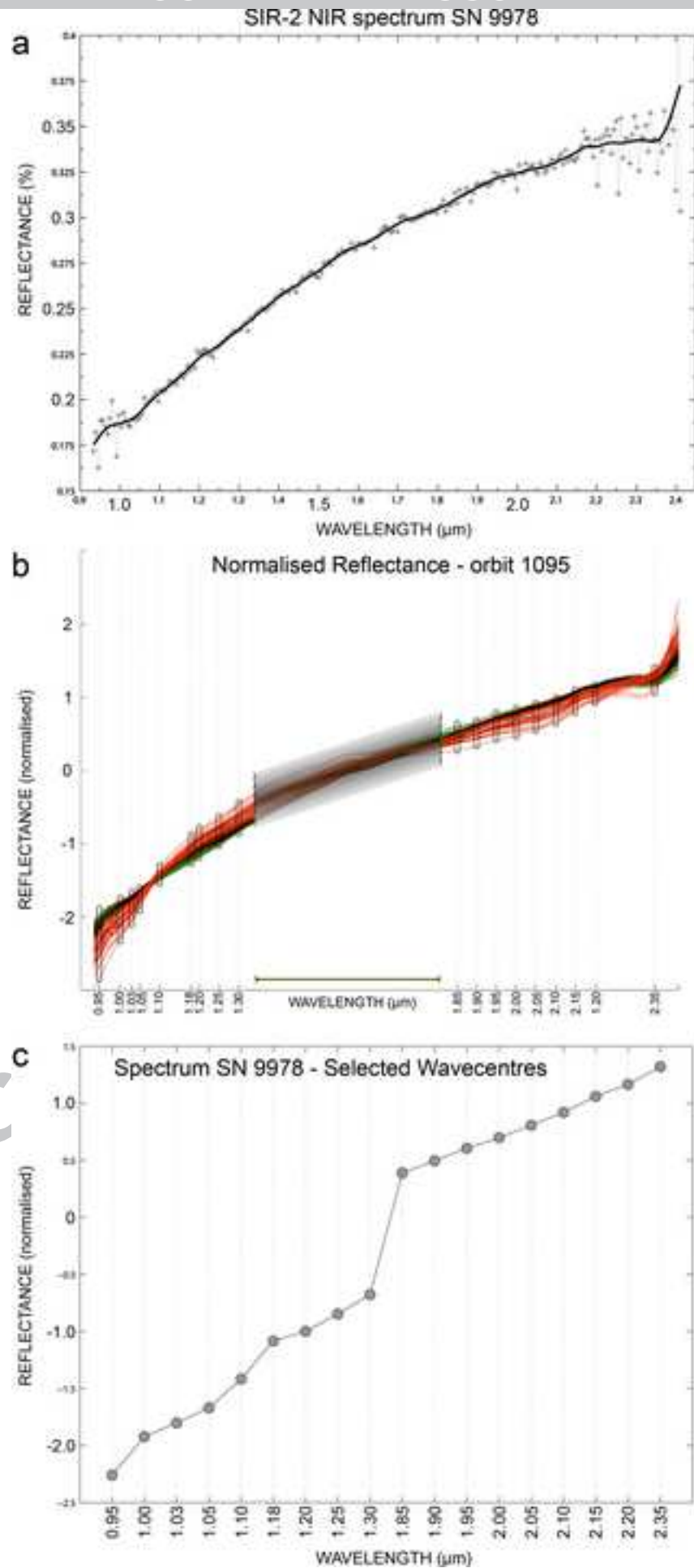


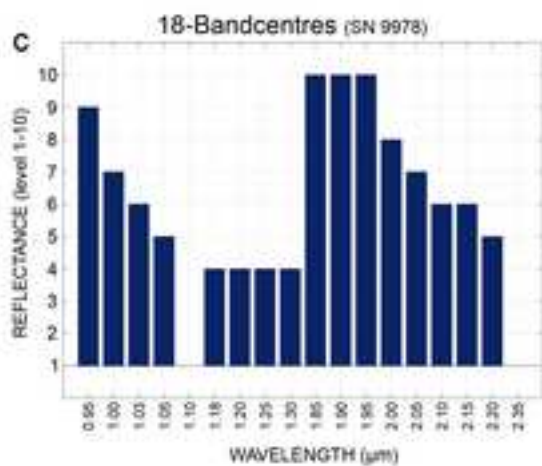
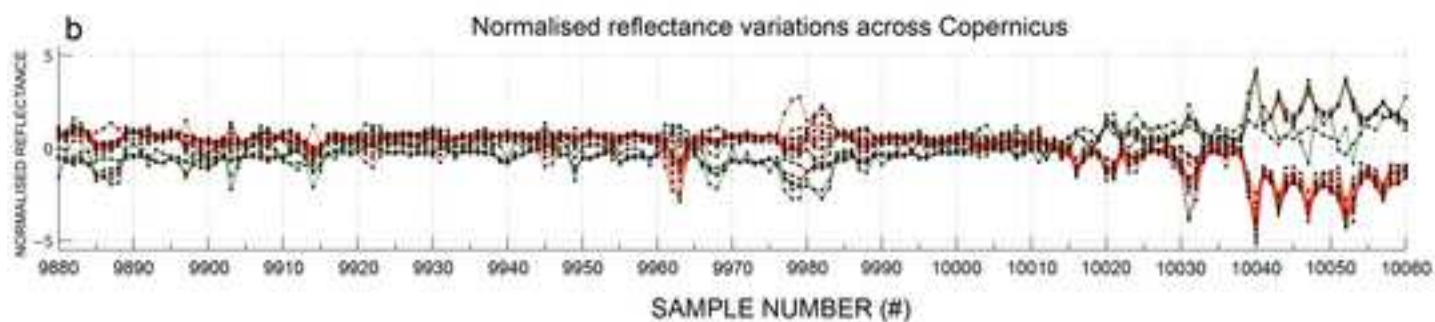
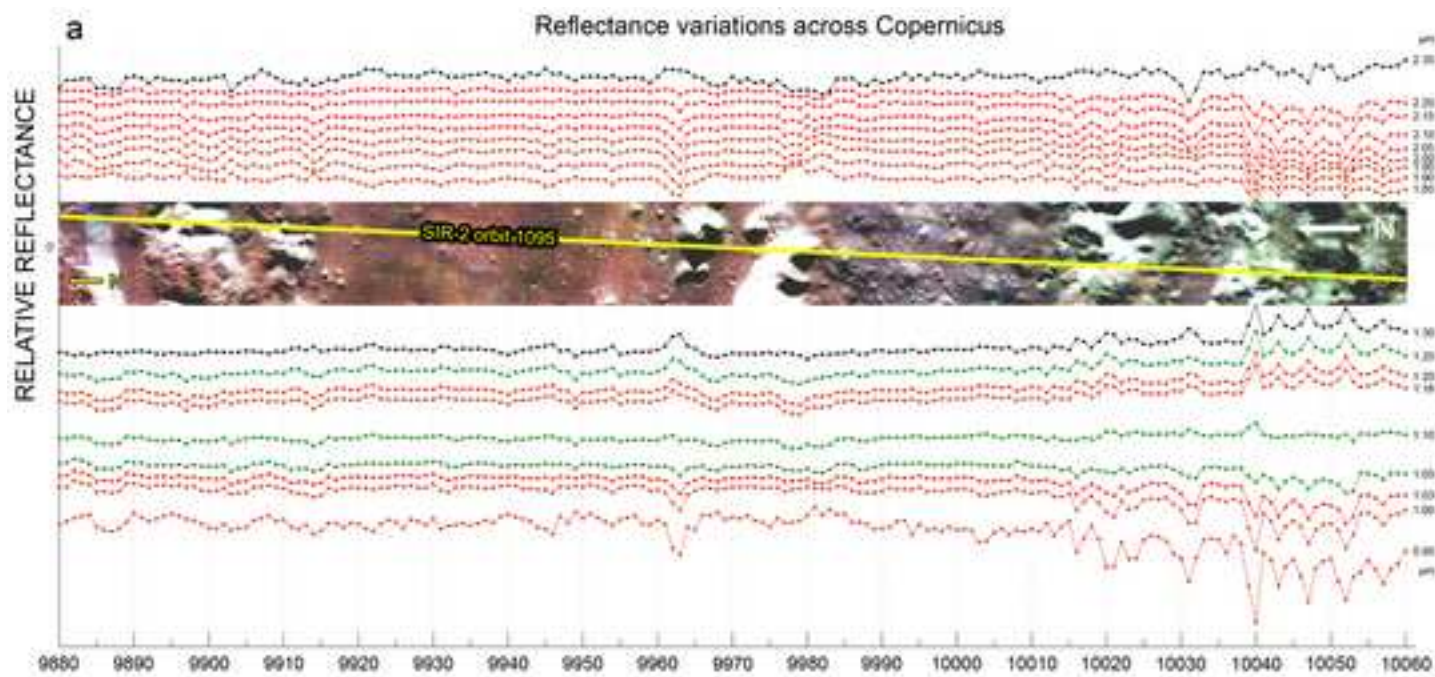


CRIPPT

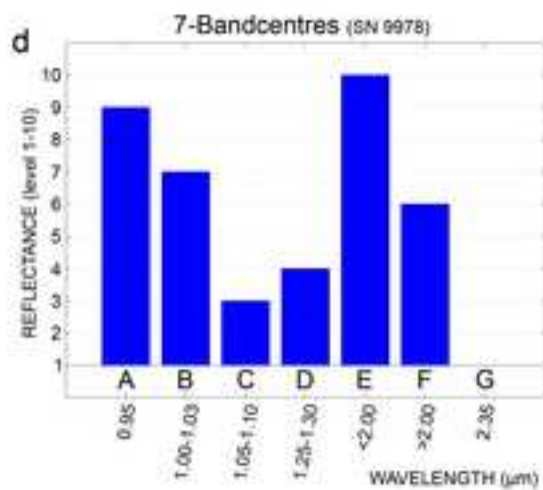
Figure_8

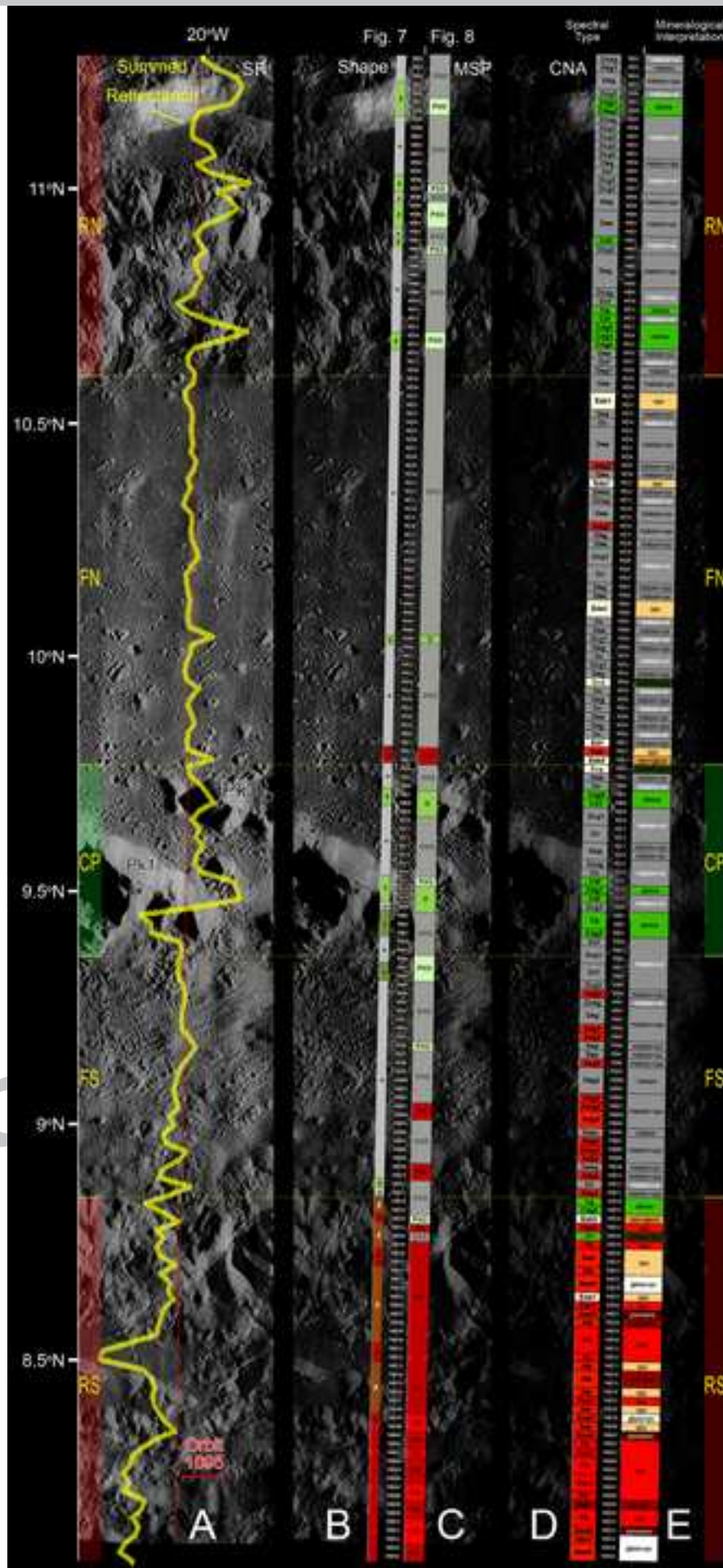


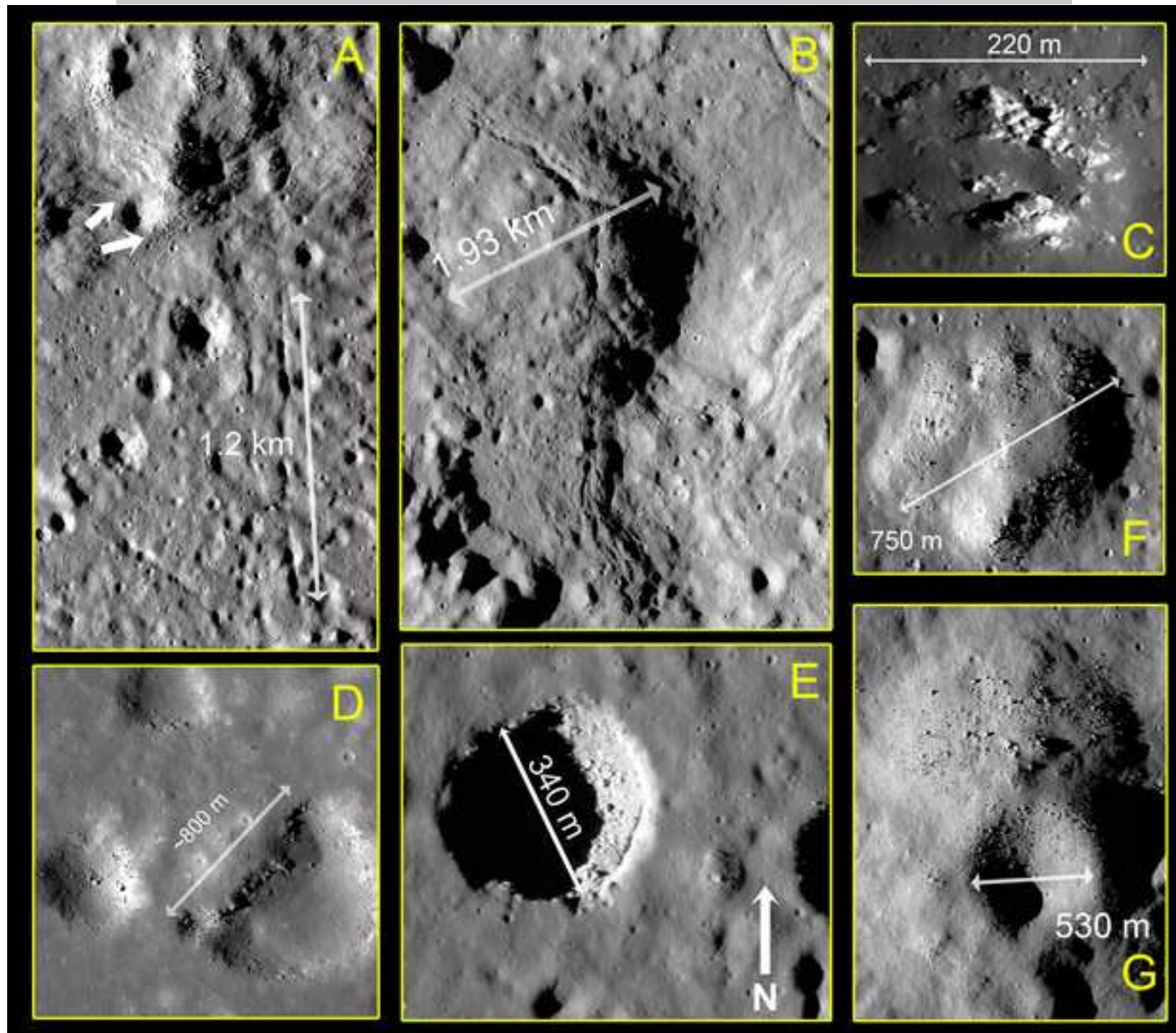


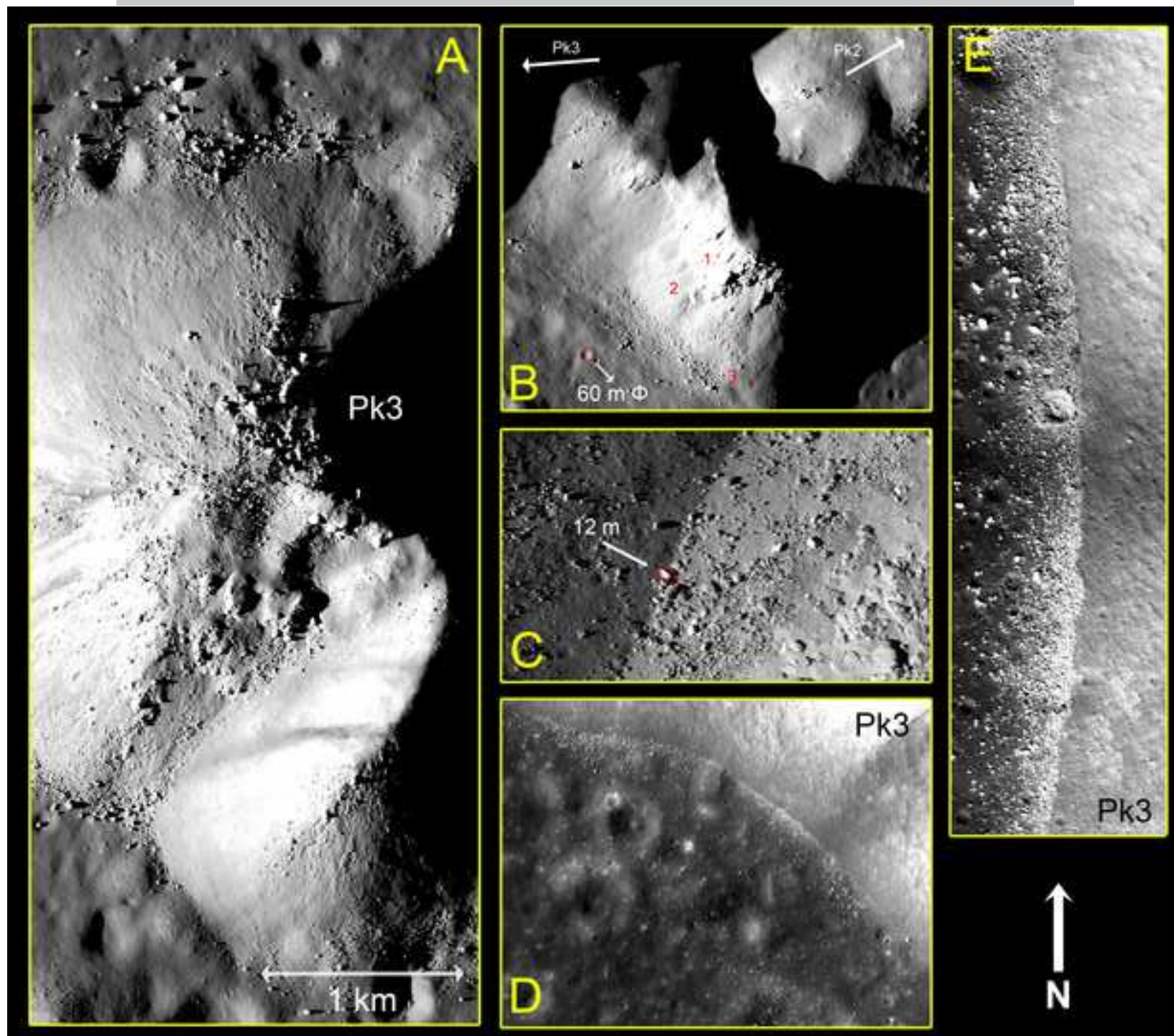


Absorption feature
Strong \leftrightarrow Weak









Index Name	Mineral index	Formulation (<i>R</i> = Reflectance % value at given band-centre, in μm)
OL-INDEX	Olivine	$\frac{R_{1.616}}{0.1 \times R_{1.053} + 0.1 \times 1.201 + 0.4 \times R_{1.329} + 0.4 \times 1.468} - 1$
LCP-INDEX	Low-Ca Pyroxene (opx)	$\frac{R_{1.329} - R_{1.053}}{R_{1.329} + R_{1.053}} \times \frac{R_{1.329} - R_{1.814}}{R_{1.329} + R_{1.814}}$
HCPX-INDEX	High-Ca Pyroxene (cpx)	$\frac{R_{1.468} - R_{1.053}}{R_{1.468} + R_{1.053}} \times \frac{R_{1.468} - R_{2.067}}{R_{1.468} + R_{2.067}}$

Table 1

SN	Fig. 7	Fig. 8	Spectral Type	Mineralogical Interpretation
9882		Dca9	mature+ol	
9883		Dag1	mature	
9884		Deg	mature+opx	
9885		Dca9	mature+ol	
9886	a	Dca9	mature+ol	
9887		Cdg1	olivine	
9888		Cda91		
9889		Dca9	mature+ol	
9890		Dca9	mature+ol	
9891		Dca9	mature+ol	
9892	a	Dca9	mature+ol	
9893		Dca9	mature+ol	
9894		Dca9	mature+ol	
9895		Dca9	mature+ol	
9896		Dca9	mature+ol	
9897	a	PXO	Dca9	mature+ol
9898		Dca9	mature+ol	
9899	a	Dca9	mature+ol	
9900		Dca9	mature+ol	
9901		Dea	mature+px	
9902	a	Dca9	mature+ol	
9903	a	Dca9	mature+ol	
9904		Dca9	mature+ol	
9905		Dca9	mature+ol	
9906		Dca9	mature+ol	
9907		Dca9	mature+ol	
9908		Dca9	mature+ol	
9909		Dca9	mature+ol	
9910		Dca9	mature+ol	
9911		Dca9	mature+ol	
9912		Dca9	mature+ol	
9913		Dca9	mature+ol	
9914		Dca9	mature+ol	
9915	a	PXO	Dca9	mature+ol
9916		Dca9	mature+ol	
9917		Dca9	mature+ol	
9918		Dca9	mature+ol	
9919		Dca9	mature+ol	
9920		Dca9	mature+ol	
9921		Dca9	mature+ol	
9922		Dca9	mature+ol	
9923		Dca9	mature+ol	
9924		Dca9	mature+ol	
9925		Dca9	mature+ol	
9926		Dca9	mature+ol	
9927		Dca9	mature+ol	
9928		Dca9	mature+ol	
9929		Dca9	mature+ol	
9930		Dca9	mature+ol	
9931		Dca9	mature+ol	
9932	a	Dca9	mature+ol	
9933		Dca9	mature+ol	
9934		Dca9	mature+ol	
9935		Dca9	mature+ol	
9936		Dca9	mature+ol	
9937		Dca9	mature+ol	
9938		Dca9	mature+ol	
9939		Dca9	mature+ol	
9940		Dca9	mature+ol	
9941		Dca9	mature+ol	
9942		Dca9	mature+ol	
9943		Dca9	mature+ol	
9944		Dca9	mature+ol	
9945		Dca9	mature+ol	
9946		Dca9	mature+ol	
9947		Dca9	mature+ol	
9948		Dca9	mature+ol	
9949		Dca9	mature+ol	
9950	a	Dca9	mature+ol	
9951		Dca9	mature+ol	
9952		Dca9	mature+ol	
9953		Dca9	mature+ol	
9954		Dca9	mature+ol	
9955		Dca9	mature+ol	
9956	a	Dca9	mature+ol	
9957		Dca9	mature+ol	
9958		Dca9	mature+ol	
9959		Dca9	mature+ol	
9960		Dca9	mature+ol	
9961		Dca9	mature+ol	
9962		Dca9	mature+ol	
9963	a	PXO	Dca9	mature+ol
9964		Dca9	mature+ol	
9965		Dca9	mature+ol	
9966		Dca9	mature+ol	
9967		Dca9	mature+ol	
9968		Dca9	mature+ol	
9969		Dca9	mature+ol	
9970		Dca9	mature+ol	
9971		Dca9	mature+ol	
9972		Dca9	mature+ol	
9973	a	Dca9	mature+ol	
9974		Dca9	mature+ol	
9975		Dca9	mature+ol	
9976		Dca9	mature+ol	
9977		Dca9	mature+ol	
9978	a	PXO	Dca9	mature+ol
9979		Dca9	mature+ol	
9980		Dca9	mature+ol	
9981		Dca9	mature+ol	
9982		Dca9	mature+ol	
9983		Dca9	mature+ol	
9984		Dca9	mature+ol	
9985		Dca9	mature+ol	
9986		Dca9	mature+ol	
9987		Dca9	mature+ol	
9988		Dca9	mature+ol	
9989		Dca9	mature+ol	
9990		Dca9	mature+ol	
9991		Dca9	mature+ol	
9992		Dca9	mature+ol	
9993		Dca9	mature+ol	
9994		Dca9	mature+ol	
9995		Dca9	mature+ol	
9996		Dca9	mature+ol	
9997		Dca9	mature+ol	
9998		Dca9	mature+ol	
9999		Dca9	mature+ol	
10000		Dca9	mature+ol	
10001		Dca9	mature+ol	
10002		Dca9	mature+ol	
10003		Dca9	mature+ol	
10004		Dca9	mature+ol	
10005		Dca9	mature+ol	
10006		Dca9	mature+ol	
10007		Dca9	mature+ol	
10008		Dca9	mature+ol	
10009		Dca9	mature+ol	
10010		Dca9	mature+ol	
10011		Dca9	mature+ol	
10012	a	Dca9	mature+ol	
10013		Dca9	mature+ol	
10014		Dca9	mature+ol	
10015		Dca9	mature+ol	
10016	a	PXO	Dca9	mature+ol
10017		Dca9	mature+ol	
10018		Dca9	mature+ol	
10019		Dca9	mature+ol	
10020		Dca9	mature+ol	
10021		Dca9	mature+ol	
10022		Dca9	mature+ol	
10023		Dca9	mature+ol	
10024		Dca9	mature+ol	
10025		Dca9	mature+ol	
10026		Dca9	mature+ol	
10027		Dca9	mature+ol	
10028		Dca9	mature+ol	
10029		Dca9	mature+ol	
10030		Dca9	mature+ol	
10031		Dca9	mature+ol	
10032		Dca9	mature+ol	
10033		Dca9	mature+ol	
10034		Dca9	mature+ol	
10035		Dca9	mature+ol	
10036		Dca9	mature+ol	
10037		Dca9	mature+ol	
10038		Dca9	mature+ol	
10039		Dca9	mature+ol	
10040		Dca9	mature+ol	
10041		Dca9	mature+ol	
10042		Dca9	mature+ol	
10043		Dca9	mature+ol	
10044		Dca9	mature+ol	
10045		Dca9	mature+ol	
10046		Dca9	mature+ol	
10047		Dca9	mature+ol	
10048		Dca9	mature+ol	
10049		Dca9	mature+ol	
10050		Dca9	mature+ol	
10051		Dca9	mature+ol	
10052		Dca9	mature+ol	
10053		Dca9	mature+ol	
10054		Dca9	mature+ol	
10055		Dca9	mature+ol	